

VISUALIZATION AND LOCALIZATION OF INTERVENTIONAL DEVICES WITH  
MRI BY SUSCEPTIBILITY MAPPING

A Dissertation

by

YING DONG

Submitted to the Office of Graduate and Professional Studies of  
Texas A&M University  
in partial fulfillment of the requirements for the degree of

DOCTOR OF PHILOSOPHY

Chair of Committee,	Jim X. Ji
Committee Members,	Steve M. Wright
	Mary P. McDougall
	Costas N. Georghiades
Head of Department,	Miroslav M. Begovic

August 2015

Major Subject: Electrical Engineering

Copyright 2015 Ying Dong

## ABSTRACT

Recently, interventional procedures can be performed with the visual assistance of MRI. However, the devices used in these procedures, such as brachytherapy seeds, biopsy needles, markers, and stents, have a large magnetic susceptibility that leads to severe signal loss and distortion in the MRI images and degrades the accuracy of the localization. Right now, there is no effective way to correctly identify, localize and visualize these interventional devices in MRI images.

In this dissertation, we proposed a method to improve the accuracy of localization and visualization by generating positive contrast of the interventional devices using a regularized  $L_1$  minimization algorithm. Specifically, the spin-echo sequence with a shifted 180-degree pulse is used to acquire high SNR data. A short shift time is used to avoid severe phase wrap. A phase unwrapping method based on Markov Random Field using Highest-Confidence-First algorithm is proposed to unwrap the phase image. Then the phase images with different shifted time are used to calculate the field map. Next,  $L_1$  regularized deconvolution is performed to calculate the susceptibility map. With much higher susceptibility of the interventional devices than the background tissue, the interventional devices show positive-contrast in the susceptibility image.

Computer simulations were performed to study the effect of the signal-to-noise ratio, resolution, orientation and size of the interventional devices on the accuracy of the results. Experiments were performed using gelatin and tissue

phantom with brachytherapy seeds, gelatin phantoms with platinum wires, and water phantom with titanium needles. The results show that the proposed method provide positive contrast images of these interventional devices, differentiate them from other structures in the MRI images, and improves the visualization and localization of the devices.

## ACKNOWLEDGEMENTS

I would like to thank my committee chair, Dr. Ji, for his guidance and advise in my Ph.D study. He discusses my problems, guides my research, revises my paper and tries his best to provide me financial aid. He teaches me every aspect in my research and life. I am very grateful for being his student. Without his guidance and support, I could not finish my Ph.D. study.

I would also like to thank my committee members, Dr. Wright and Dr. McDougall, for their guidance and support throughout the course of this research. They are very knowledgeable about Magnetic Resonance Imaging, and they teach me very useful knowledge about MRI. I still remember the course to build a MRI from scratch, which increases my fundamental understanding of MRI and benefits my research.

I would like to thank my committee member Dr. Georghiades. As an associate dean for research in ECEN department, he is very busy. Even so, he spends time talking to me face to face, trying to understand my research topics. I appreciate his kindness and help.

Thanks also go to my friends and colleagues, Shuo Feng, Ching-hua Ching, John Bosshard, Ke Feng, Neal Hollingsworth, Katie Moody, Edwin Eigenbrodt, Tao Yang and Aydin Eresen for the help during my research. They help me acquire the data, provide me many useful opinions, help me solve many problems. Without them, I may not finish my Ph.D. study on time.

I would like to thank Tammy Carda, Anni Bruncker and other department faculty and staff for the help during my Ph.D. study. They make my time at Texas A&M University a great experience.

Thanks to my mother and father for their encouragement, support and love for the last 29 years. They take care of me from every detail, they understand me when I make mistakes, they support me for the unpopular decision I made, and they unconditionally love me and do not ask any return. I feel very lucky and happy to have them as my parents. They are the reason for me to keep improving myself.

Last but not least, I would like to thank my husband for his patience and love. We know each other for about 14 years, and we are in a relationship for more than 7 years. He accompanies my entire Ph.D. study, providing advice when I face problems, cheering me up when I feel upset. I am very thankful that I met him and married him.

## NOMENCLATURE

MRI	Magnetic Resonance Imaging
SNR	Signal-to-Noise Ratio
MRF	Markov Random Field
HCF	Highest Confidence First
SGM	Susceptibility Gradient Mapping
SUMO	SGM with Original Resolution
coRASOR	Center-out Radial Sampling with Off-resonance Reception
CS	Compressive Sensing
TV	Total Variation

## TABLE OF CONTENTS

	Page
ABSTRACT .....	ii
ACKNOWLEDGEMENTS .....	iv
NOMENCLATURE .....	vi
TABLE OF CONTENTS .....	vii
LIST OF FIGURES .....	x
LIST OF TABLES .....	xiv
CHAPTER I INTRODUCTION .....	1
1.1 Thesis Outline .....	3
CHAPTER II INTERVENTIONAL DEVICES .....	5
2.1 Introduction of Interventional Devices .....	5
2.2 Imaging Assistant of Interventional Procedure with MRI .....	7
2.3 Related Research .....	8
2.4 Methodology .....	11
CHAPTER III FIELD MAPPING USING PHASE IMAGES .....	13
3.1 High SNR Data Acquisition with Spin-echo Sequence with Shifted 180° Pulse ..	13
3.1.1 Pulse sequence.....	13
3.1.2 Parameters selection .....	15
3.2 Phase Unwrapping Using a Markov Random Field Modeling .....	15
3.2.1 Synopsis.....	15
3.2.2 Introduction .....	16
3.2.3 Theory .....	19
3.2.4 Image preparation.....	22
3.2.5 Segmentation .....	23
3.2.6 Phase modeling using MRF .....	25
3.2.7 Model optimization using HCF .....	28
3.3 Field Mapping .....	31
3.4 Results .....	32
3.4.1 Simulated data .....	32

3.4.2 In-vivo MRI brain images .....	35
3.4.3 Phase image with cutline .....	37
3.4.4 Phase unwrapping for interventional devices .....	40
3.5 Discussions .....	40
3.6 Conclusions .....	42
CHAPTER IV LOCALIZATION OF BRACHYTHERAPY SEEDS IN MRI BY MAPPING THE SUSCEPTIBILITY .....	43
4.1 Introduction .....	43
4.1.1 Difficulty in localization of brachytherapy seeds .....	43
4.1.2 Related work to provide positive contrast .....	44
4.2 Theory .....	46
4.3 Methods .....	48
4.3.1 Data acquisition using SE sequence with shifted 180° pulse .....	48
4.3.2 Susceptibility mapping with regularized $L_1$ minimization .....	48
4.3.3 Computer simulations .....	50
4.3.4 Experimental data acquisition .....	52
4.4 Results .....	54
4.4.1 Computer simulations .....	54
4.4.2 Experiments with tissue phantoms .....	57
4.5 Discussions .....	65
4.6 Conclusions .....	67
CHAPTER V LOCALIZATION OF LARGE-SIZE INTERVENTIONAL DEVICES AND SPEEDUP .....	68
5.1 Localization of Other Interventional Devices with Larger Size .....	68
5.1.1 Introduction of larger interventional devices .....	68
5.1.2 Data simulations and experimental acquisitions with full-k-space data .....	70
5.1.3 Reconstruction using CS with composite sparsifying transform to reduce acquisition time .....	71
5.1.4 Reconstruction using full k-space data .....	72
5.2 Image Reconstruction Improvement Using Compressive Sensing with Composite Sparsifying Transforms .....	76
5.2.1 Introduction of compressive sensing .....	76
5.2.2 Compressive sensing MRI with combined sparsifying transforms .....	78
5.2.3 Data preparation and performance evaluation .....	81
5.2.4 Results .....	84
5.2.5 Combined the compressive sensing and interventional devices localization .....	89
5.3 Discussions .....	92
5.4 Conclusions .....	95



CHAPTER VI CONCLUSIONS .....	97
REFERENCES .....	99

## LIST OF FIGURES

	Page
Fig. 2.1 The flow chart of the proposed method .....	11
Fig. 3.1 The spin-echo sequence with shifted 180° pulse .....	14
Fig. 3.2 (a) A wrapped phase generated from a low-pass-filtered complex random field and (e) shifted with $\pi/3$ . The phase unwrapped using (b, f) 2D Goldstein Branch Cut Phase Unwrapping method, and (c, g) 2D Quality Guided Phase Path Following Phase Unwrapping method, and (d, h) Phase unwrap method provided by MATLAB. ....	20
Fig. 3.3 (a) A wrapped phase with open-ended cutline, and (b) its high-pass filtered phase using (c) a high-pass filter in k-space. ....	21
Fig. 3.4 Flow chart of the proposed phase unwrapping method. ....	22
Fig. 3.5 Illustration of 6-neighborhood system and the six cliques that contains pixel (x,y,z), marked as dashed ellipses. ....	27
Fig. 3.6 Illustration of the neighborhood of regions: the orange and green regions are both the neighbors of blue region. Pixel 1 is used twice for phase difference calculation between orange region and blue region, and pixel 2 is used once for phase difference calculation between green region and blue region. ....	28
Fig. 3.7 Phase unwrapping a simulated MRI phase image: (a) simulated image with phase wrapping; (b) segmented regions with intensity corresponding to the region index; (c) unwrapped phase image using the proposed method; (d) simulated image with noise yields SNR = 1.5; (e) segmented regions with intensity corresponding to the region index without passing through a high-pass filter; (f) unwrapped phase image using the proposed method. ....	33
Fig. 3.8 Computation time for the proposed method, the method in [26], the PUMA method, and the $Z\pi M$ method with SNR ranges from 1.5 to 100. ....	35
Fig. 3.9 Phase unwrapping an in-vivo brain MRI image: (a) original phase image; (b) unwrapping phase image by the proposed method; (c) unwrapping phase image by the method in [26]; (d) unwrapping phase image by the PUMA method; and (e) unwrapping phase image by the $Z\pi M$ method. ....	37

Fig. 3.10 Phase wrapping an image that violates the smoothness constraint: (a) original phase image; the image contains regions that are challenging to unwrap (see text) as pointed by the arrows, (b) inset illustrating the problem in (a). There is no correct solution as the phase unwrapping will result differently if it follows a clockwise path or a counterclockwise path. The unwrapped phase image shown in (c-g) is from the proposed method, the pole-guided-cutline method, the method in [26], the PUMA method, and the $Z\pi M$ method, respectively.....	39
Fig. 3.11 Phase unwrapping of brachytherapy seeds. (a) The wrapped phase; (b) the unwrapped phase using the proposed method.....	40
Fig. 4.1 (a) The structure of a dummy STM 1251 I-125 brachytherapy seed; (b) The dimension and susceptibility of the materials in the seed [6].....	52
Fig. 4.2 The simulated images (representative slice) and the corresponding results using the proposed method from the slices perpendicular to the seeds: (top row) seeds perpendicular to $B_0$ , (bottom row) seeds parallel to $B_0$ ; (a)(f) magnitude image, (b)(g) phase image, (c)(h) field map, (d)(i) susceptibility map calculated by the proposed method, and (e)(j) maximum intensity projection rendering of susceptibility maps. ....	55
Fig. 4.3 Reconstructions of a seed at different SNR in the simulated studies: (first row) SNR = 8, (second row) SNR = 4 and (third row) SNR = 2; (a) (f) (k) magnitude images, (b) (g) (l) phase images, (c) (h) (m) mask generated by thresholding the magnitude images, (d) (i) (n) positive contrast images from the proposed method, and (e) (j) (o) reference of the true seed location. ....	56
Fig. 4.4 Reconstruction of a seed with images simulated at different resolutions: (first row) 1.5mm, (second row) 1mm, and (third row) 0.5mm; (a) (f) (k) magnitude images, (b) (g) (l) phase images, (c) (h) (m) masks, (d) (i) (n) positive contrast images created using the proposed method, and (e) (j) (o) reference of the true seed image location. ....	57
Fig. 4.5 A representative axial slice reconstructed from a gelatin phantom with two dummy seeds: (a) magnitude image from the spin echo acquisition, (b) phase image from the acquisition with $T_{shift} = 0.3ms$ , (c) calculated field map, (d) positive contrast image using the proposed method.....	59
Fig. 4.6 The positive contrast images created by (a) the proposed method, and (b) the SUMO method; (c): zoomed-in 1D cross-section near the left seed, indicated by the line segments in (a) and (b); (d) MIP reconstruction from the 3D reconstruction by the proposed method; (e) MIP reconstruction from images processed by the SUMO method.....	60

Fig. 4.7 Upper row: Images from the first tissue phantom experiment: (a) photo of the phantom; (b) magnitude image; (c) phase image with $T_{shift} = 0$ ms; and (d) phase image with $T_{shift} = 0.3$ ms. As shown, in addition to the three seeds, a bamboo toothpick (upper red arrow) is used to simulate capillary and a plastic stick (lower green arrow) is used to simulate natural cavities and voids. Lower row: Reconstructions using two different methods: (e) calculated field map; (f) mask M; and (g) positive contrast image generated by the proposed method, and (h) by the SUMO method. Note that seeds are placed in the phantom such that they are perpendicular to the B0 field. ....	62
Fig. 4.8 Images from the second tissue phantom experiment: (a) photo of the phantom with the spacing between the seeds labeled; (b) magnitude image; and (c) positive contrast image generated by the proposed method. ....	63
Fig. 5.1 (a) Photo of the platinum wires in a gelatin phantom; (b) MR magnitude image; (c) phase image with $T_{shift} = 0$ ms, (d) phase image with $T_{shift} = 0.2$ ms; (e) calculated field map; and (f) susceptibility image from the proposed method. The edges of the images are cropped for better visualization. ....	73
Fig. 5.2 The results from the computer simulation. (a) Magnitude image; (b) Phase image when $T_{shift} = 0.2$ ms; (c) the ideal field map without noise, with +/-10ppm contour labeled; and (d) the susceptibility map calculated using the proposed method. ....	74
Fig. 5.3 (a) Photo of the biomarker needle in water phantom; (b) magnitude image; (c) phase image with $T_{shift} = 0.1$ ms; (d) field map calculated from the phase images; and (e) susceptibility map from the proposed method. The edges of the images are cropped for better visualization. ....	75
Fig. 5.4 The reference images reconstructed from the fully sampled k-space data. (a) breast MRI, (b) brain image, and (c) abdominal image. Details inside the regions highlighted in rectangular boxes are shown in Figs. 5.7 and 5.8. ....	83
Fig. 5.5 A typical L-curve for (a) single regularization term and (b) linear summation of two regularization terms. ....	84
Fig. 5.6 Sparsifying transforms applied to the brain image: (a) wavelet transform, (b) finite-differences, (c) composite (wavelet and finite-difference) transform of second data set (real and imaginary), and (d) pixel distribution of the three transforms, which shows that the proposed composite transform yields improved sparsity. ....	85
Fig. 5.7 CS reconstructions of the highlighted regions in Fig. 5.4 of: (a) breast image; (b) brain image; and (c) abdominal image. Different columns show	

(from left to right): reference images, reconstructions using TV, Wavelet, linear summation of TV and Wavelet, and the proposed method (last column). On each reconstruction, $\lambda_1$ is the weight for TV term, $\lambda_2$ is the weight for wavelet, and $\lambda$ is the weight for the proposed method.....	86
Fig. 5.8 The error images between the reconstructed images and the reference images. The rows and columns correspond to those in Fig. 5.7.....	87
Fig. 5.9 Magnitude (first row) and phase (second row) images of center slices with Tshift = -0.3ms, reconstructed with (first column) full k-space data, and (second column) 20 radial lines, which corresponding to 28% of total k-space data. ....	90
Fig. 5.10 Field maps (first row) and susceptibility maps (second row) of center slices with Tshift = -0.3ms, reconstructed with (first column) full k-space data, and (second column) 20 radial lines, which corresponding to 28% of total k-space data. ....	91

## LIST OF TABLES

	Page
Table 2-1 The common size, shape, material and susceptibility of the interventional devices .....	6
Table 3-1 The detail procedure of the HCF method .....	31
Table 3-2 The error rate (%) of the proposed method, the method in [26], the PUMA method and the $Z\pi M$ method. ....	34
Table 4-1 The half-intensity regions and reduction rates in the computer simulations and phantom experiments. Data from representative slices shown in Figs. 4.2~4.8 .....	64
Table 5-1 Normalized mean square errors for finite-differences, wavelet, linear summation and the proposed method .....	88
Table 5-2 Averaged single and total computational time (s) for finite-differences, wavelet, linear summation and the proposed method .....	89

# CHAPTER I

## INTRODUCTION

Magnetic Resonance Imaging (MRI) is a non-invasive imaging technique to investigate the anatomy and function of the body. Since its invention in early 1970's, it has been rapidly developed and widely used in many clinical and experimental studies. Thousands of millions of researchers dedicate their effort on every detail and aspect of MRI, including hardware design, pulse sequence design, image quality improvement, and clinical applications, etc.

With superior contrast between soft tissues, MRI has become a noninvasive gold standard in many clinical applications, such as brain tumor diagnosis, coronary heart disease, and breast imaging, etc. Researchers are making effort on combining MRI with other applications. One effort is to use MRI to visually assist interventional procedures, such as brachytherapy, angioplasty, and invasive procedure, etc.

However, to safely combine these procedures with the assistance of MRI, the devices and instruments has to be specially designed and made in order to be magnetic compatible. Titanium is the most common material that is used. Other materials include gold, silver, copper, aluminum, nickel, platinum and compounds. These material usually have susceptibility of  $-100\sim 100\text{ppm}$ . Within this range, the material will not experience any magnetic force.

Though these materials are MR compatible, they still have much higher absolute susceptibility than the tissue. The high absolute susceptibility alters the nearby magnetic

field, resulting severe signal decay due to fast dephasing. Therefore, there is a big black hole in the magnitude image, and rapid phase wrap in the phase image around the high susceptible objects. The black hole in the magnitude image is usually several times larger than the actual size of the devices. And it may be confused with other low signal structures in the tissue, which may cause confusion. Therefore, the black hole, as known as negative contrast, hinders the accuracy of the procedure, which may result in severe consequence.

In recent years, many researches have been done to turn the negative contrast into positive contrast. These methods include pulse sequence design, such as 3D Center-Out Radial Sampling with Off-resonance Reception (coRASOR) and Inversion-Recovery with ON-resonant water suppression (IRON) [1, 2], and post-processing methods, such as Susceptibility Gradient Mapping (SGM) and SGM using the original resolution [3, 4].

A property of these materials is the high absolute susceptibility. We propose to map the susceptibility of the interventional devices and background tissue to provide positive-contrast of the devices.

The contribution of this thesis is to propose a new method to generate positive contrast of the interventional devices using a regularized  $L_1$  minimization algorithm to improve the accuracy of localization and visualization. Instead of applying gradient echo sequences commonly used in susceptibility mapping, we propose to use the spin-echo sequence with a shifted 180-degree pulse to acquire high SNR data. A short shift time is used to avoid severe phase wrap. A new phase unwrapping method based on Markov



Random Field using Highest-Confidence-First algorithm is proposed to unwrap the phase image. The phase unwrapping method is capable of dealing with open-ended fringelines, which are quite common with rapid phase unwrapping caused by high susceptible objects. Then the unwrapped phase images from at least two different shifted time are used to calculate the field map. Next,  $L_1$  regularized deconvolution is performed to calculate the susceptibility map. With much higher susceptibility of the interventional devices than the background tissue, the interventional devices show positive-contrast in the susceptibility image.

## **1.1 Thesis Outline**

Chapter 2 is a brief introduction to interventional devices. It provides the necessary basic background about different interventional procedures and the devices used in these procedures. The difficulties of imaging these devices using MRI are addressed. Related researches to provide positive contrast of these devices are introduced. The limitations of these works are discussed. Then, I present the motivation of solving this problem and the logic flow of the proposed method.

Chapter 3 introduces the data acquisition using spin-echo sequence with a shifted 180-degree pulse. Then the phase unwrapping method using a Markov random field is presented. The simulation and experimental results are presented and discussed.

Chapter 4 talks about the localization of the brachytherapy seeds using  $L_1$  regularized deconvolution. The method is introduced and the results are presented.

Improved localization and differentiation are achieved using the proposed method for brachytherapy seeds.

Chapter 5 extends the method in Chapter 4 to larger interventional devices. New difficulties are present due to the larger size of highly susceptible objects. Furthermore, we try to speedup the acquisition time by combining the proposed method with compressive sensing. We also introduce a reconstruction method of compressive sensing with composite sparsifying transform. Comparing to conventional CS with linear summation of sparsifying transforms, this method can provide similar or better reconstruction results with shorter calculation time. The simulation results and experimental results are presented. The proposed method is capable to deal with larger size high susceptible interventional devices.

Finally, we will sum up the work in Chapter 6.

## CHAPTER II

### INTERVENTIONAL DEVICES

#### **2.1 Introduction of Interventional Devices**



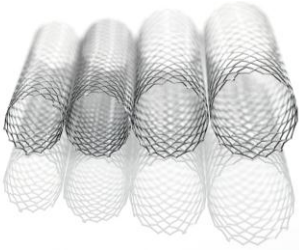

The common interventional devices include brachytherapy seeds, needles, stents, and markers.

Brachytherapy is to cure the cancer by inserting radioactive material into the tumor, to provide highly localized radioactive therapy without affecting the healthy tissue. During and after the surgery of brachytherapy, the location of the brachytherapy seeds needs to be identified because the location information will indicate how the radioactive material distributes. Another application is the angioplasty. Angioplasty is to mechanically widen narrowed or obstructed arteries using a mesh tube, i.e. stent, to prevent or counteract a disease-induced, localized flow constriction. The stent insertion and evaluation of the treatment requires image assistance.

These interventional procedures have been widely used, because they can provide minimized physical trauma, reduced infection rates, decreased recovery time and medical expense.

The common size, shape, material and susceptibility of the devices are listed in Table 2.1. The grey part means the material is not suitable to be scanned by MRI.

Table 2-1 The common size, shape, material and susceptibility of the interventional devices

Devices	Diameter	Length	Material	Susceptibility (ppm)	Pictures
Brachytherapy seeds	0.8mm	4.5mm	Ti	182	
			Cu	-9.63	
			Ni	116	
			Al	20.7	
			Au	-34	
Brachytherapy needles	1.27mm (outer)	20cm	Ti	182	
	0.84mm (inner)		Al	20.7	
			Plastic	-9.3	
Stents	3.0mm	~20mm	Co & Cr	320	
	81μ~120μ thickness		Stainless steel	3520~6700	
			Pt & Cr	279 & 320	
			Ti	182	
Markers	15mm	3.5mm thickness	Vinyl plastisol, Vaseline	-6.65~-5.95	

The market of interventional devices is huge. Take brachytherapy products for example, the US sales were \$240 million in 2008 and expected to \$1979 million by 2016. Implantable prostate seeds were the largest market segment with sales of 121.5

million in 2008, comprising 51% of total brachytherapy sales. Other important brachytherapy market segments are partial breast irradiation with sales of \$41.7 million in 2008. With this big market, there are great needs to provide accurate visualization and localization to assist the physicians to plan, perform and evaluate the therapy.

## **2.2 Imaging Assistant of Interventional Procedure with MRI**

Without measurable harmful effects and good soft-tissue contrast [5], magnetic resonance imaging has become a gold standard for many applications. However, due to the high magnetic field, metal material should be operated with extreme caution, especially the interventional devices. Though some interventional devices are now made of MR-compatible material, such as titanium, the high susceptibility will still introduce a high local field changes and thus introduce image artifacts.

Though the metallic material will introduce artifacts, we sometimes need to locate the exact location of the metallic material, which is extremely useful in interventional radiology. MRI is superior to other imagine modalities due to its high contrast between soft-tissues. Therefore, to combine MRI and the interventional procedure is of great needs and interests.

However, there are many problems associated with this combination. Because MRI is a high magnetic field, it places specific requirements and limitations to the MRI. Any ferromagnetic materials inside the MRI room are harmful, so the surgery tools and the implanted devices to perform the interventional radiology should be MR compatible. Usually, titanium and other paramagnetic materials can be used in the MRI. However,

the susceptibility of these materials are in the range of 20~200 ppm, much higher than soft-tissue (-9ppm). This kind of material won't experience detectable forces or torques. However, they increase the magnetic field variation, resulting in faster dephasing of the spin in and around the materials [6]. Therefore, the signal decays much faster than the background tissue, introducing a black hole around the interventional devices.

The signal loss will spread out from the location of the interventional devices to neighboring region, and results in location uncertainty of several millimeters. This artifact will hinder the accuracy of the surgery, especially in the angioplasty where the diameter of the vein/artery is only several millimeters. Another drawback of the negative contrast (the interventional devices appear to be dark compared to the background tissue) is that it increases the difficulty in differentiating the devices with other dark features in MR magnitude images. The features include artery (excited blood flow moves out of field of view) and natural cavity. One example of this problem is shown in [7].

To solve this problem, it is critical to create positive contrast of these interventional devices. The positive contrast can highlight the objects and thus differentiate them with background tissue. And this positive contrast can also provide accurate localization of the interventional devices.

### **2.3 Related Research**

Many existing methods have addressed the problem to provide positive contrast of paramagnetic structures. A new pulse sequence, inversion-recovery with ON-resonant

water suppression (IRON), employs a spectrally-selective on-resonant saturation prepulse to provide positive contrast [2]. Another 3D imaging technique, applying center-out radial sampling with off-resonance reception (co-RASOR), is also proposed to provide positive contrast for small paramagnetic objects [1]. Later on, a new method based on co-RASOR is proposed by using a single acquisition rather than on multiple acquisitions, and is able to achieve increased efficiency and signal intensity [8]. However, these techniques require new pulse sequences and it is hard to implement in the clinical scanner. Another draw back of these methods is that the positive contrast it provided is by shifting the signal from neighboring region, rather than imaging the objects themselves.

Some post-processing methods are also employed without changing the pulse sequence and acquisition trajectories. One simple method is to threshold the high-pass filtered phase image to achieve positive contrast, though it is used for cellular imaging [9]. In Susceptibility Gradient Mapping (SGM) method, the local susceptibility gradient is calculated using a short-term Fourier transform (STFT) for every pixel over a small window, which is then used to selectively turn the negative contrast into a positive contrast [3]. However, this method reduces the spatial resolution because the susceptibility gradient is assumed to be a constant over the window length. An improved version of SGM, named SUMO, using a truncated filter in k-space instead of STFT is proposed to maintain the original resolution [4]. Though the above methods can provide positive contrast of the metallic material, all of them are directly based on the phase information or field map. However, the phase information or field map spread out from

the brachytherapy seeds to the surrounding tissues. As a result, the positive contrast images these methods achieved still don't reveal the exact location of the seeds. Even the error is only several millimeters, it will result in unevenly distributed radioactive material which reduces the accuracy of the surgery [6].

To achieve the positive contrast of the interventional devices with exact location, we can take advantage of the high susceptibility of the metallic components. Therefore, the method we are going to propose should address the following problems:

Aim 1: To generate accurate field map from the phase images with high SNR;

Aim 2: To generate the positive contrast of the interventional devices with accurate localization information;

Aim 3: Validate the location accuracy by comparing with existing methods using phantom/ex-vivo data.

To address the above 3 aims, a method similar to quantitative susceptibility mapping (QSM) is applied to calculate the susceptibility of the seeds and background tissue [10]. With much stronger signal-to-noise ratio (SNR), Spin Echo sequence with shifted  $180^\circ$  pulse is used, instead of Gradient Echo sequence. Then a phase unwrapping method is proposed based on Markov Random Field to accurately unwrap the phase and reveal the field variation. Then to overcome the low SNR and low data fidelity due to the large signal decay around the seeds, we propose to add a weighting matrix and masking matrix around the seeds to correctly locate the seeds. Numerical simulation and phantom experiments were performed to test the proposed method. We also functionalized SUMO method and compare the result of positive contrast.



## 2.4 Methodology

To address the above 3 aims, the method we proposed to provide positive contrast of the interventional devices includes three steps, as shown in Fig. 2.1.

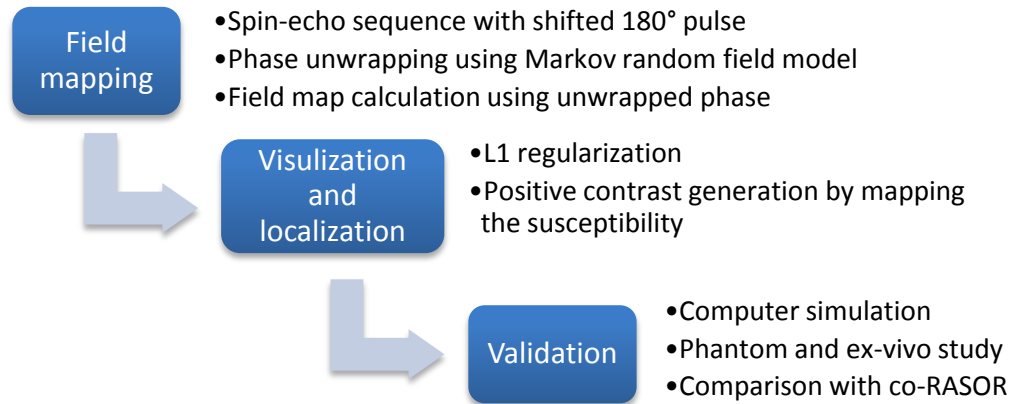


**Fig. 2.1 The flow chart of the proposed method**

The first step is to acquire the field mapping: (1) two or more MR images with spin-echo sequence with shifted  $180^\circ$  pulse, because spin-echo images have better SNR than gradient-echo images; (2) the phase images are unwrapped using phase unwrapping method based on Markov random field model; (3) then the field map is calculated based on the unwrapped phase images. The second step is to provide the positive contrast and localization of the interventional devices with L1 regularization. The last step is to validate the proposed method by performing simulation and experimental study. The computer simulation will perform tests on different size, shape and susceptibility of the interventional devices to study the feasibility of the proposed method. Then experimental data will be acquired from both MRSL 4.7T Varian scanner and TIPS 3T

Siemens scanner with gelatin phantom and animal/tissue phantom. To compare the proposed method with existing well-established method, the 3D center-out radial sampling with off-resonance reception (co-RASOR) will also be performed on MRSL to test the accuracy of the localization.

## CHAPTER III

### FIELD MAPPING USING PHASE IMAGES

#### **3.1 High SNR Data Acquisition with Spin-echo Sequence with Shifted 180° Pulse**

##### ***3.1.1 Pulse sequence***

Unlike other susceptibility related method, the proposed method doesn't use gradient-echo related sequence. The reason to choose spin-echo sequence over gradient-echo sequence is because of the high SNR.

Spin-echo sequence is well known as superior capability to overcome field inhomogeneity and susceptibility.

In the conventional spin-echo sequence, the 90° pulse will tip the magnetization into x-y plane, then the dephasing began due to the dephasing gradient, field inhomogeneity and susceptibility. The 180° pulse will reverse the effect of the later two, thus the signal refocuses at TE. With shifted 180° pulse, suppose the 180° pulse is shifted to the left by time  $\Delta t$ . Now the time between 90° and 180° pulse is  $TE/2 - \Delta t$ , as shown in Fig. 3.1, thus the dephasing will recover at  $TE - 2\Delta t$ . But the echo appears at TE due to the frequency encoding gradient. Thus the dephasing due to the field inhomogeneity and susceptibility will dephase again after its recover. It is equivalent to have the effect of field inhomogeneity and susceptibility for  $2\Delta t$ , where  $\Delta t$  can be in the order of 0.1ms or even smaller.

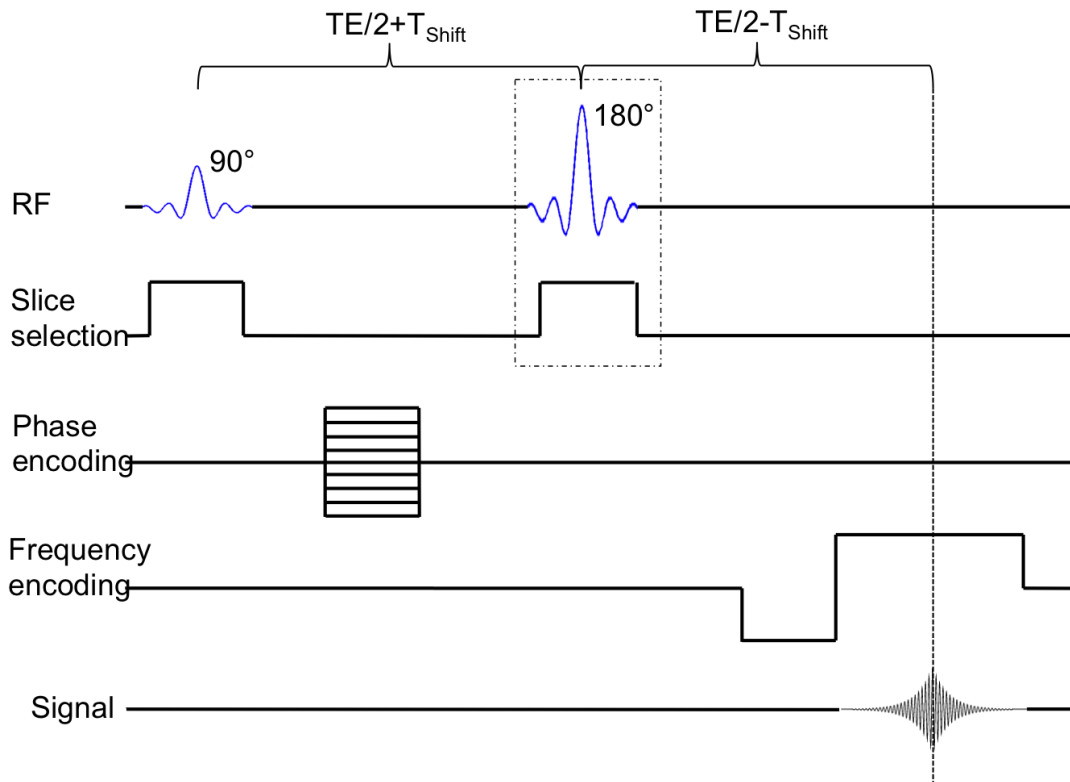


**Fig. 3.1 The spin-echo sequence with shifted 180° pulse**

The advantage of the spin-echo with shifted 180° pulse is that, in gradient echo sequence, the effect of field inhomogeneity and susceptibility will in effect for the whole TE. However, for high susceptibility for interventional device, the field variation is much larger. The phase will be wrapped many times for such a long time as TE. The field map recovered from gradient-echo sequence will not be accurate.

Recently, gradient echo sequence with ultra-short TEs has been proposed to be used in this application. However, it requires rapid switching time for the gradients, and it is not accessible to some of the MRI machines.

In summary, by choosing the spin-echo with shifted  $180^\circ$  pulse, we are able to acquire high quality data with the absence of paramagnetic materials. And the sequence is well defined and easily accessible in the MRI system or with little modification.

### ***3.1.2 Parameters selection***

As stated before,  $\Delta t$ , together with the field map, controls the amount of phase into the image. If  $\Delta t$  is too small, the  $2\pi$  range is not fully utilized and the field map calculation may be degraded because of noise. In the contrast, if  $\Delta t$  is too large, the phase will unwrapped to fast and there might be more than  $2\pi$  change between two neighboring pixels and phase unwrapping method cannot correctly unwrap the phase. Therefore,  $\Delta t$  should be carefully selected in order to correctly calculate the field map from phase image.

To study this, first the field map for brachytherapy seeds and a needle is simulated.

## **3.2 Phase Unwrapping Using a Markov Random Field Modeling**

### ***3.2.1 Synopsis***

Phase unwrapping is a critical step to utilize the information embedded in phase images in many applications of Magnetic Resonance Imaging (MRI). However, robust and effective phase unwrapping remains a challenge when open-ended outline problems show up in the phase images. This chapter presents a novel phase unwrapping method, which is suitable to unwrap the phase with and without open-ended outline. Specifically,

the image is segmented into regions where within each region the phase is not wrapped. Then, the phase is modeled as Markov Random Field variable on the region level. The magnitude image is used as a guideline to locate the outline in the phase image if there is any. The phase is unwrapped between different regions by minimizing the global energy using a highest-confidence-first algorithm. Results on simulated and experimental MRI images show that the proposed method provides similar or improved phase unwrapping than the Phase Unwrapping Max-flow/min-cut (PUMA) method, the  $Z\pi$ M method and the pole-guided-outline phase unwrapping method.

### **3.2.2 Introduction**

Phase images can provide useful information in many applications of Magnetic Resonance Imaging (MRI). For example, phase images can indicate the  $B_0$  inhomogeneities, the inherent chemical shift of the object, the object's magnetic susceptibility, and the velocity of blood flow, or tissue motions [11]. Thus, it can be used to shim the magnetic field, map the susceptibility, and measure the flow.

To reveal the embedded information, phase unwrapping is necessary because only the wrapped phase, i.e., phase constrained to  $[-\pi, \pi)$ , is available from a complex-valued MRI images. Mathematically, phase unwrapping is to determine the correct phase  $\phi$  from its wrapped phase  $\psi$ , where

$$\psi = \text{mod}(\phi + \pi, 2\pi) - \pi \quad (3.1)$$

where  $\text{mod}(\cdot)$  is the modulus operator. Without additional restrictions, the problem of phase unwrapping is ill-posed. Therefore a smoothness condition, named Itoh condition, is widely used as a constraint, which assumes the adjacent phase difference satisfied

$$|\Delta\phi_{x,y}| \leq \pi \quad (3.2)$$

where  $\Delta\phi_{x,y}$  is the phase changes at location  $(x,y)$  with respect to its neighbors [12].

A variety of phase unwrapping algorithms have been developed during last several decades. Broadly speaking, they can be classified into four major categories: path following methods [13, 14], minimum-norm methods [15, 16], parametric modeling [17, 18], Bayesian and regulation methods [19, 20]. For a comprehensive review of phase unwrapping methods, the reader is referred to [21]. For a comparison of different methods, the reader is referred to [22, 23].

Bayesian and regularization methods model the phase as random variables, and the maximum a posteriori (MAP) probability is a popular statistical criterion for optimality. Markov Random Field (MRF) model based phase unwrapping [19, 24-27] is a class of unique algorithms that belongs to this category. In these methods, the smoothness constraint is incorporate in the Markovian property of the phase in a neighborhood, or, clique. A potential or energy function is defined on the whole image based on the MRF model whose minimization leads to phase unwrapping solutions. This approach provides a general mechanism for modeling local contextual dependence, with the flexibility to handle effectively both smooth and nonsmooth features.

In practice, the MRF models and optimization algorithms differ. For example, the Phase Unwrapping Max-flow/min-cut (PUMA) method inherits the idea and solves the optimization problem by graph cut techniques [25]. It provides an exact energy minimization for the clique potentials that are convex, and devises an approximate solution for the nonconvex clique potentials due to their discontinuity preserving ability.

The method in [26] provides a series of dynamic programming connected by the iterated conditional modes (ICM) to reduce the computational complexity of the optimization procedure. The method breaks the image into blocks, and uses dynamic programming in each block. By setting the block to be a 1-D array, the 2-D optimization problem is simplified to a series of 1-D ones. This method can solve the phase unwrapping efficiently. The  $Z\pi$ M method [24] performs the phase unwrapping and smoothing at the same time. It iteratively calculates the MAP absolute phase estimate with a discrete optimization step (Z-step) and an ICM step ( $\pi$ -step).

These methods have been successfully used in various applications. Nevertheless, the phase images can be complicated when open-ended cutline appear in the phase image. The open-ended cutline is an edge of  $2\pi$  phase jump around which a path can be found that phase changes gradually/smoothly. The reason of the open-ended cutline is insufficient resolution, flow, or noise. The presence of the open-ended cutline is unpredictable and it violates the Itoh condition. Therefore a phase unwrapping method that can handle both the regular phase image and the ones with open-ended cutline is preferred. However, only a few phase unwrapping methods address this problem. [11] introduces a pole-guided-cutline phase unwrapping method which designs specific for this application. The curl of the phase is calculated to identify poles that are formed by  $2 \times 2$  pixels with only one phase wrap. By setting the phase to 0, the poles move following the cutline until two poles reach and annihilated. Then the phase of the whole image is shifted by some degree, and a new cutline is chased. A score map is obtained by repeating this process. And the cuts are found by finding the skeleton of the score map.



As stated by the author, once the cuts are found, the phase unwrapping can be performed in any fashion.

This chapter presents a novel phase unwrapping method, taking advantage of the magnitude image. There are two unique features of the method: I. the segmented regions are modeled as MRF variables instead of using pixel-level MRF only, which significantly improves the computation efficiency; II. it uses a highest-confidence-first (HCF) optimization method and the information from magnitude image to locate the cutlines with the most reliability. The simulated and experimental MRI images are used to test the proposed method. The results show that the proposed method provides similar or improved phase unwrapping than the method in [26], the Phase Unwrapping MAX-flow/min-cut (PUMA) method and the  $Z\pi$ M method.

### **3.2.3 Theory**

A cutline is the borderline where  $2\pi$  phase jump appears. A closed cutline can be easily removed from the wrapped phase image by adding or subtracting  $2\pi$  to every pixel within the cutline. Many conventional phase unwrapping methods just assume every cutline in a phase image is closed, because it is straightforward and efficient for most of the cases. However, when the cutline is open-ended, these methods will produce obvious wrong results, as shown in Fig. 3.2 (b-d).

The phase unwrapping becomes complicated when open-ended cutline exist. (i) It is difficult to figure out whether the cutline is closed or open-ended. The conventional methods will. (ii) The cutline will move when a background phase shift is applied. Fig. 3.2 (a, e) are the phase image from a same complex random field, and  $\pi/3$  shift is applied

on (a) to achieve (e). The cutline moves and the unwrapping method provided by MATLAB provides different results. (iii) A phase jump will appear in the unwrapped phase image, however, there are no obvious criteria to locate the phase jump.

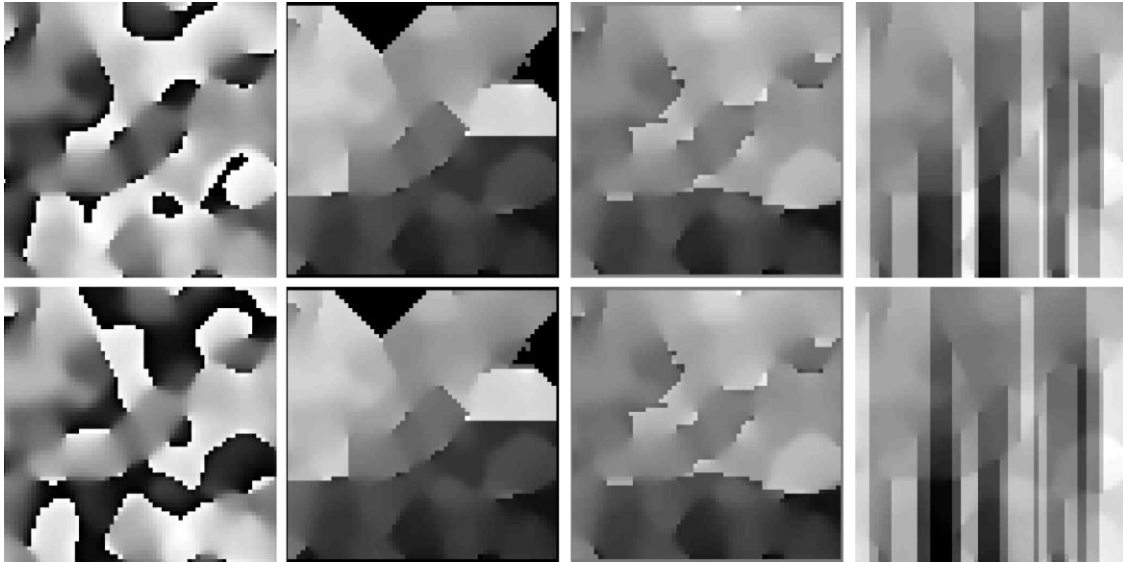


**Fig. 3.2 (a) A wrapped phase generated from a low-pass-filtered complex random field and (e) shifted with  $\pi/3$ . The phase unwrapped using (b, f) 2D Goldstein Branch Cut Phase Unwrapping method, and (c, g) 2D Quality Guided Phase Path Following Phase Unwrapping method, and (d, h) Phase unwrap method provided by MATLAB.**

The open-ended outline in MRI is due to several reasons. The resolution is low which cannot provide smooth change over rapid phase changing area. (ii) Noise introduces randomly fluctuation, especially in low signal area.

The open-ended cutline cannot be neglected because it cannot be removed by high-pass filter. As shown in Fig. 3.3(a), a wrapped phase image from a 3D fast spin-echo sequence with a 180-degree inversion recovery prepulse. A clear open-ended cutline is shown in the skull. Fig. 3.3(b) shows the processed phase with a high-pass filter, as shown in Fig. 3.3(c), applying in the k-space. The open-ended cutline is not removed. Therefore, it is critical to handle the open-ended cutline correctly in order to acquire accurate susceptibility weighted imaging and field mapping.

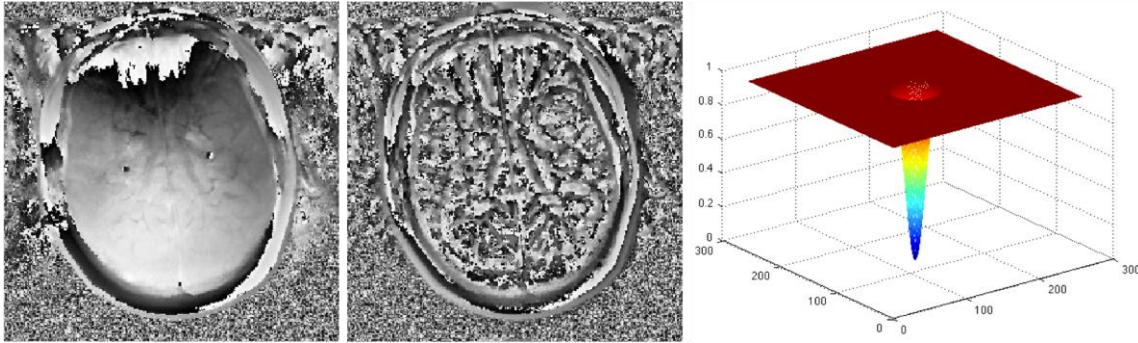


**Fig. 3.3 (a) A wrapped phase with open-ended cutline, and (b) its high-pass filtered phase using (c) a high-pass filter in k-space.**

Many cutline detection phase unwrapping methods are proposed for Interferometric synthetic aperture radar (InSAR), and thus no magnitude image available for them to use. Since there is a correlation between the phase image and magnitude image in MRI, it is a predominance to take advantage of the magnitude image. The physical prior of the proposed method is to assume that the open-ended cutline happens at the boundary of the tissue.

The basic idea of the proposed method is to segment the phase image into regions within which the phase is not wrapped, and then perform phase unwrapping between different regions using a highest-confidence-first algorithm to optimize the MRF model. Fig. 3.4 presents the flow chart of the proposed phase unwrapping method. Details of the steps will become clear in the rest of this section.

### 3.2.4 Image preparation

This is a preprocessing step to properly scale the phase image and remove the redundant areas in the image. For example, if the phase data is saved in a DICOM format with 16 bits, it needs to be scaled to be within  $[-\pi, \pi)$ .

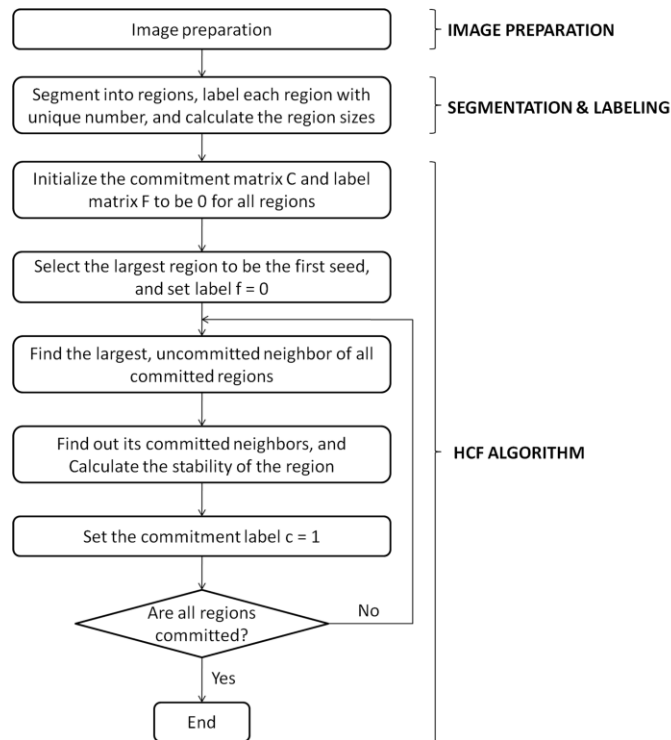


**Fig. 3.4 Flow chart of the proposed phase unwrapping method.**

In MRI, parts of the image are background, for example, area outside the anatomy. These regions should be removed for improved efficiency and reliability. To do so, high-contrast magnitude image can be used if it exists, or the phase image itself can be used. In this chapter, a Gaussian filter and thresholding is applied after the magnitude image is normalized. Then, morphological operators, such as erosion and dilation, are used to fill the holes in the image and to clean out isolated dots [28].

### **3.2.5 Segmentation**

The purpose of the image segmentation stage is to identify the region within which the phase is not wrapped. Segmentation is carried out in two steps.

The first step is to mask out the background, in order to eliminate unreliable data and reduce unnecessary calculation. High-contrast magnitude image can be used if it is exist, or the phase image itself. A Gaussian filter is first utilized to overcome the effect of noise, and then threshold segmentation is applied. The holes in the structure are filled. Isolated dots in the background are cleaned out. Only one connected region is left for next step. The operations are performed using morphological operators erode and dilate.

The second step is to segment the phase structure, to eliminate phase wrap in each region. This can be achieved by restricting the range of the phase within one region to be smaller than  $2\pi$ .

The segmentation can be carried out by many methods. In this work, a 2-threshold method [29] is used for simplicity. Specifically, the pixels in the phase image is first classified into  $T$  categories,  $\psi \in [-\pi, \frac{(-T+2)\pi}{T})$ ,  $\psi \in [\frac{(-T+2)\pi}{T}, \frac{(-T+4)\pi}{T})$ , ..., and

$\psi \in [1 - \frac{(T-2)\pi}{T}, \pi)$ , using a simple thresholding procedure. When  $T = 2$ , the phase should follow the Itoh condition in order to be correctly unwrapped. However, if there is cutlines,  $T > 2$  should be used. Other segmentation methods could also be used, at the price of longer computational time.

When the image is noisy, the thresholding method could result in many segments. A high pass filter is applied before the segmentation to find out the noisy pixels and eliminate by adding or subtracting  $2\pi$ .

After segmentation, a matrix, named category matrix, with the same size of the phase image, is used to record the category of each pixel. Then, an indexing process is carried out to segment the pixels into several connected regions [30]. Basically, the algorithm makes two left-to-right, up-to-down passes over a binary image: the first pass is to assign temporary indices by checking only the left and up pixels, and to record equivalences if both the left and up pixels belong to a connected region. The second pass is to confirm the temporary indices with no equivalence, to replace the higher ones by their lower equivalence, and to squeeze the unused indices. The procedure is repeated  $T$  times, each time for a specific category in the category matrix.

After the segmentation and indexing process, the image is segmented into  $R$  regions. The region index for a specific pixel  $(x, y, z)$  is denoted as  $m_{x,y,z}$ , where

$$1 \leq m_{x,y,z} \leq R.$$

### 3.2.6 Phase modeling using MRF

For each pixel, the correct phase  $\phi$ , i.e., unwrapped phase, and the wrapped phase  $\psi$  are related by

$$\phi_{x,y,z} = \psi_{x,y,z} + 2\pi \cdot f_{x,y,z} \quad (3.3)$$

where  $(x,y,z)$  is the location of the pixel, and  $f_{x,y,z}$  is an integer where

$f_{x,y,z} \in \{-L, \dots, -1, 0, 1, \dots, L\}$  with  $L$  being determined by the number of wraps in the phase image.

Let  $\Psi = \{\psi_{x,y,z} \mid x=1,2,\dots,X; y=1,2,\dots,Y; z=1,2,\dots,Z\}$  and

$\Phi = \{\phi_{x,y,z} \mid x=1,2,\dots,X; y=1,2,\dots,Y; z=1,2,\dots,Z\}$ , where  $X*Y*Z$  is the size of the image. The phase unwrapping problem can be posed as finding  $\Phi$  given  $\Psi$ . In the MRF model in this work, the correct phase is treated as a random variable that can only take finite possible values as defined in Eq. 3.3 [31, 32]. With this formulation, the correct phase can be estimated using a maximum a posteriori (MAP) estimator,

$$\hat{\Phi} = \arg \max_{\Phi} p(\Phi \mid \Psi) = \arg \max_{\Phi} p(\Phi) p(\Psi \mid \Phi) \quad (3.4)$$

where  $p(\Phi)$  denotes the prior probability, and  $p(\Psi \mid \Phi)$  is the likelihood function [26].

Because the value of  $\Psi$  for a given  $\Phi$  is determined by Eq. 3.3, Eq. 3.4 becomes

$$\hat{\Phi} = \arg \max_{\Phi} p(\Phi) \quad (3.5)$$

Hammersley-Clifford theorem [31, 33] states that an MRF has an equivalent Gibbs distribution where

$$p(\Phi) \propto \exp(-U(\Phi)) \quad (3.6)$$

where  $U(\Phi)$  is an energy function. Therefore, the MAP problem of Eq. 3.5 is transferred to an energy minimization problem.

$$\hat{\Phi} = \arg \min_{\Phi} U(\Phi) \quad (3.7)$$

A variety of functions have been studied in literature. A common-used function is based on the square of the difference between adjacent pixels.

$$U(\Phi) = \sum_{\substack{1 \leq x \leq X \\ 1 \leq y \leq Y \\ 1 \leq z \leq Z}} \sum_{(x',y',z') \in N_{x,y,z}} (\phi_{x,y,z} - \phi_{x',y',z'})^2 \quad (3.8)$$

where  $N_{x,y,z}$  is the set of all neighbors of pixel  $(x,y,z)$ . A typical 6-neighborhood system is shown in Fig. 3.5. An image acquired with 2DFT is a simplified case of the image acquired with 3DFT, where  $Z=1$ . A series of multiple slice 2D images can be unwrapped repeatedly using the proposed method. Due to the fact that  $\phi_{x,y,z}$  is related to the observed and wrapped phase  $\psi_{x,y,z}$  by Eq. 3.3, the above energy function can be equally defined as

$$U(F) = \sum_{\substack{1 \leq x \leq X \\ 1 \leq y \leq Y \\ 1 \leq z \leq Z}} \sum_{(x',y',z') \in N_{x,y,z}} (\psi_{x,y,z} + 2\pi f_{x,y,z} - \psi_{x',y',z'} - 2\pi f_{x',y',z'})^2 \quad (3.9)$$

where  $F = \{f_{x,y,z} \mid x = 1, 2, \dots, X; y = 1, 2, \dots, Y; z = 1, 2, \dots, Z\}$ . This energy function serves as the quantitative measure of the global quality of the solution and also as a guide to the search for a minimal solution [31].



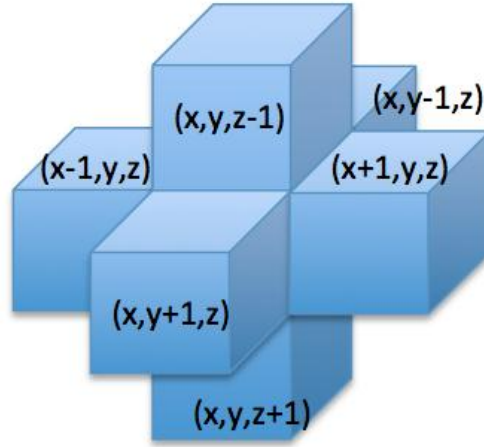


**Fig. 3.5 Illustration of 6-neighborhood system and the six cliques that contains pixel  $(x,y,z)$ , marked as dashed ellipses.**

A unique feature of the proposed method is the recognition that the labels  $\{f_{x,y,z}\}$  for all pixels within a specific region should be identical. Given that during the segmentation step the phase variation within a region is restricted to be  $\frac{2\pi}{T}$  where  $T \geq 3$ , it is straightforward to see that there is no phase jump larger than  $\frac{2\pi}{3}$  exists within the same region. Therefore, the integers of  $2\pi$  phase jump as described in Eq. 3.3 must be the same for all pixels in a region. Otherwise, the phase variation will be larger than  $\frac{2\pi}{3}$ .

For simplicity,  $f^m$  will be used to refer to the label for all pixels in region  $m$ . Therefore, the label of a pixel  $(x,y,z)$  is related to  $f^m$  by  $f_{x,y,z} = f^{m_{x,y,z}}$  where  $m_{x,y,z}$  is the region index. With this simplification, one can refine the energy function in Eq. 3.9 as

$$U(F) = \sum_{1 \leq m \leq R} \sum_{(x,y,z) \in B^m} \sum_{\substack{(x',y',z') \in N_{x,y,z} \\ (x',y',z') \in B^{N^m}}} (\psi_{x,y,z} + 2\pi f_{x,y,z} - \psi_{x',y',z'} - 2\pi f_{x',y',z'})^2 \quad (3.10)$$

where  $B^m$  is the set of border pixels in the  $m$ -th region,  $N_{x,y,z}$  is the set of all neighbors of pixel  $(x,y,z)$ , and  $N^m$  is the set of all neighboring regions of the region  $m$ .

The neighborhood of a region can be more complicated than that of pixels because more regions could be the neighbors of a particular region. An illustration of a possible neighborhood of regions is shown in Fig. 3.6.

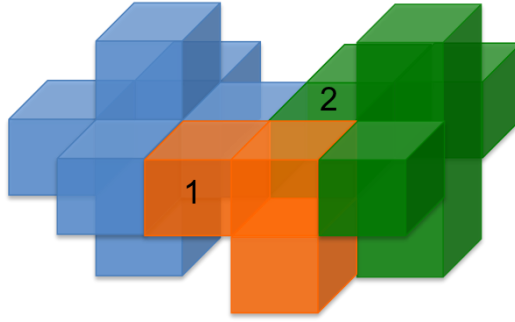


**Fig. 3.6 Illustration of the neighborhood of regions: the orange and green regions are both the neighbors of blue region. Pixel 1 is used twice for phase difference calculation between orange region and blue region, and pixel 2 is used once for phase difference calculation between green region and blue region**

### ***3.2.7 Model optimization using HCF***

With the energy function defined in Eq. 3.10, a series of energy minimization methods could be carried out to find the optimal labels  $F$ . Here we choose the highest-

confidence-first (HCF) method, a deterministic algorithm for combinatorial minimization [31, 34].

HCF uses a strategy to optimize the energy function from the least “stable” regions. These regions normally correspond to the areas with least ambiguity and small noises. The stability is determined based on the commitment status of the region and its neighbors in addition to their phase values. Specifically, a binary flag  $C = \{0,1\}$  is introduced to record the commitment status where 0 represents uncommitment and 1 commitment.  $c^m \in C$  is the commitment flag for the region  $m$ . Initially, all flags are set to zeros. Once a region is committed, it cannot go back to 0.

As an intermediate step, an energy function for the  $m$ -th region is defined as

$$E^m(f^m) = \sum_{n \in N^m} \sum_{(x,y,z) \in B^m} \sum_{(x',y',z') \in B^n} c^n (\psi^m + 2\pi f^m - \psi^n - 2\pi f^n)^2 \quad (3.11)$$

The stability of the region  $S^m$  represents the energy barrier and is defined as

$$S^m(f^m) = \begin{cases} - \min_{l \in L, l \neq l_{\min}} [E^m(l) - E^m(l_{\min})], & \text{if } c^m = 0 \\ \min_{l \in L, l \neq f^m} [E^m(l) - E^m(f^m)], & \text{if } c^m = 1 \end{cases} \quad (3.12)$$

where  $l_{\min} = \arg \min_{l \in L} E^m(l)$ . For an uncommitted region,  $S^m$  is the negative difference between the lowest and the second lowest local energies. The negative stability means there is room for improving. The greater  $|S^m|$  is, the more energy it will give out when committed. Therefore it is more confident to commit the label to be  $f^m = l_{\min}$ . For a committed region,  $S^m$  is the difference between the current local energy and the lowest possible energy due to any other label. Greater  $S^m$  indicates more stable label. The stability of a committed region could go back to negative due to the commitment of its

neighbors. Once the stability goes back to negative, the label  $f^m$  needs to change to some other values in order to be stable.

To formulate this process, let  $k = \arg \min_m S^m(f^m)$  is the least stable region. If the region  $k$  is not committed, the label of region  $k$  is committed to

$$f^k = \arg \min_{l \in L} E^k(l) \text{ when } c^k = 0 \quad (3.13)$$

If the region is already committed, change the label to a new one  $f^{k'}$  according to

$$f^{k'} = \arg \min_{l \in L, l \neq f^k} [E^k(l) - E^k(f^k)] \quad (3.14)$$

The following steps are how the HCF works. Initially,  $f^k$  is set to be 0 for all regions, which means without phase unwrapping,  $\phi^k = \psi^k$ . As defined, only the committed regions have effect on the neighbors. When no neighbor is active, the energy measure reduces to 0. Therefore, the first region to be committed needs to be assigned to serve as a seed. In this work, the largest region after segmentation is chosen to be the first, and its label is set to be 0. The label is committed by minimizing the energy  $E^k$  except for the first seed whose label is committed to be 0. Since the label of the seed region is committed, the stability of its neighbors will be updated. The stabilities of all regions are ranked and the region with smallest stability is selected to get committed next. This process repeats until all regions have non-negative stability. To illustrate the algorithm, a detailed list of steps is shown in Table 3-1.

To evaluate the performance of the proposed algorithm, the error rate (ER) and computation time is used, and comparison with the method in [26], PUMA and  $Z\pi M$  methods is conducted. The error rate is defined as the percentage of pixels for which the

unwrapped phase is different from the correct phase. The pixels in background are not processed and therefore are not taken into account in computing the ER.

*Table 3-1 The detail procedure of the HCF method*

---

Initialization:  $f^m = 0$ ,  $S^m = 0$ , and  $c^m = 0$ , for  $m = 1, 2, \dots, R$ ;

1: Select the largest region as a seed, set the label  $f^{seed} = 0$ , flag  $c^{seed} = 1$

2: Update  $S^{seed}$  and all its neighboring regions

3: Sort  $S$

4: While (the smallest stability is negative)

5: {  $k = \text{index of the region with smallest stability}$ ;

6: Set  $f^k = \min_l E^k(l)$ ;

7: Update stability of region  $m$ ,  $S^k(f^k)$ ;

8: For each  $n \in N^k$

9: {Update  $S^k(f^k)$ ;}  
 10: Sort the stability of all regions;}

---

### 3.3 Field Mapping

The Larmor frequency is proportional to the local magnetic field, resulting in difference of phase. The field map can be calculated using  $\Delta B = \frac{\psi_2 - \psi_1}{\gamma(T E_2 - T E_1)}$ . With the

correct phase, the field map can be easily achieved.

The field map is a critical step to map the susceptibility, which is extremely useful in brachytherapy MRI.

### **3.4 Results**

This computed simulations and the phase unwrapping procedure were performed offline using MATLAB (Math Works, Natick, MA). First, the normal phase images without open-ended cutline from simulation and experimental data are used to test the proposed method of handling regular phase unwrapping problem. The method in the method in [26], the PUMA method, and the  $Z\pi$ M method are used for comparison. Then, an experimental image with open-ended cutline is used to test the proposed method of handling no-solution problem. The method specific for cutline problem is also tested in this case.

#### ***3.4.1 Simulated data***

A two-dimensional parabola pattern phase was generated to simulate a normal MRI phase image without cutline. The phase is a function of distance from the center and modulus by  $2\pi$ , as shown in Fig. 3.7 (a). The image size is 128 x 128. For region segmentation, T was set to 3. The segmented regions are shown in Fig. 3.7 (b) where the intensity reflects the region index numbers. Fig. 3.7 (c) shows the unwrapped phase using the proposed algorithm. The phase decreases linearly with the radius, as expected.

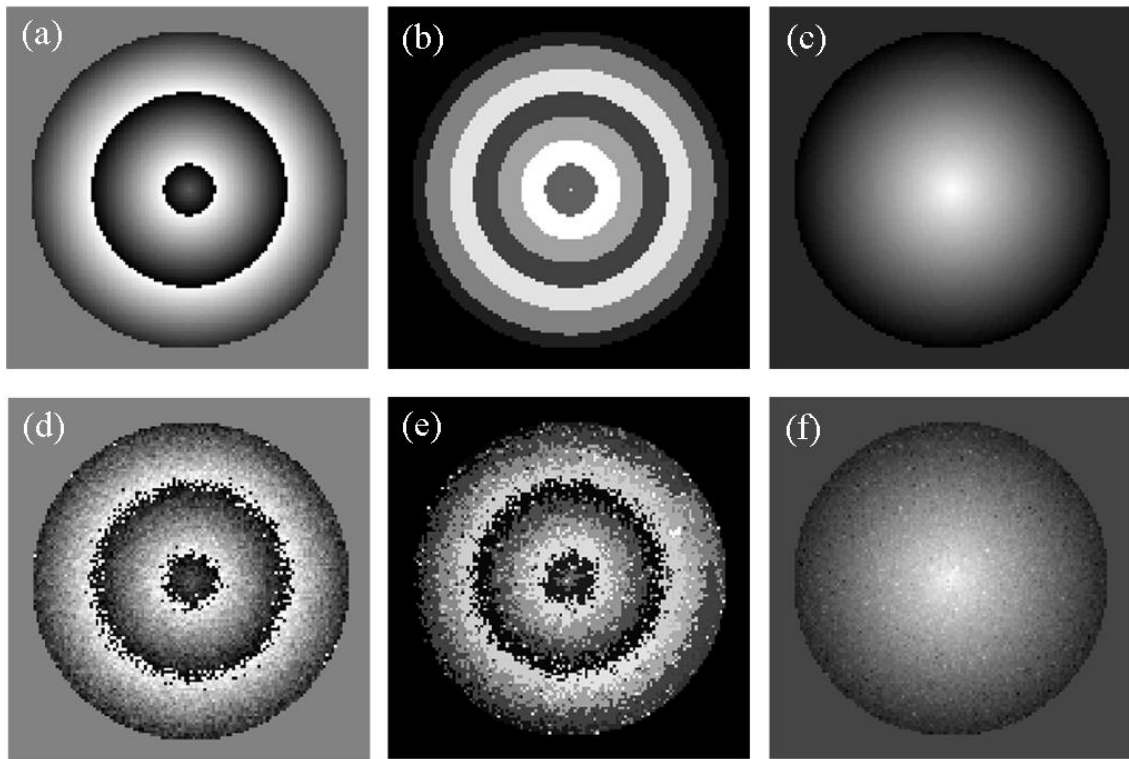


**Fig. 3.7 Phase unwrapping a simulated MRI phase image: (a) simulated image with phase wrapping; (b) segmented regions with intensity corresponding to the region index; (c) unwrapped phase image using the proposed method; (d) simulated image with noise yields  $SNR = 1.5$ ; (e) segmented regions with intensity corresponding to the region index without passing through a high-pass filter; (f) unwrapped phase image using the proposed method.**

To further demonstrate the capability of the proposed method, random variations yielding signal-to-noise-ratio (SNR) of 1.5 were added to the phase image. The added variances are uncorrelated Gaussian noise. Introduction of these variations makes phase less “smooth” and more difficult to unwrap. Fig. 3.7(d-g) is the procedure dealing with

the noisy case. The number of segments in Fig. 3.7(f) is 873, comparing to 947 in Fig. 3.7(e). The computational time is decreased accordingly. Fig. 3.7(g) shows the proposed method unwraps the noisy image correctly.

To compare with other phase unwrapping methods, SNR of 20, 2.0, 1.5, and 1.0 were added to the phase image. The phase images were unwrapped by the proposed method, the method in [26], the PUMA method and the  $Z\pi M$  method. The ER of the results were calculated. To calculate ER, the true phase was defined as the parabola pattern with Gaussian variations. The ER from all four methods is listed in Table 3-2.

*Table 3-2 The error rate (%) of the proposed method, the method in [26], the PUMA method and the  $Z\pi M$  method.*

<b>SNR</b>	<b>RB-MRF</b>	<b>Method in [26]</b>	<b>PUMA</b>	<b><math>Z\pi M</math></b>
20	0	0	0	0
2	0	0.03	0	0
1.5	0	0.07	0.02	0.03
1	0.49	1.02	0.98	0.54

Fig. 3.8 (a) provides the computation time of the four methods with image size 128\*128 and SNR ranges from 1.5 to 100. The figure shows the proposed method has the comparable computational time. The computational time for the proposed method increases for low SNR. This is because the computation complexity of the proposed method is proportional to the number of segmented regions.



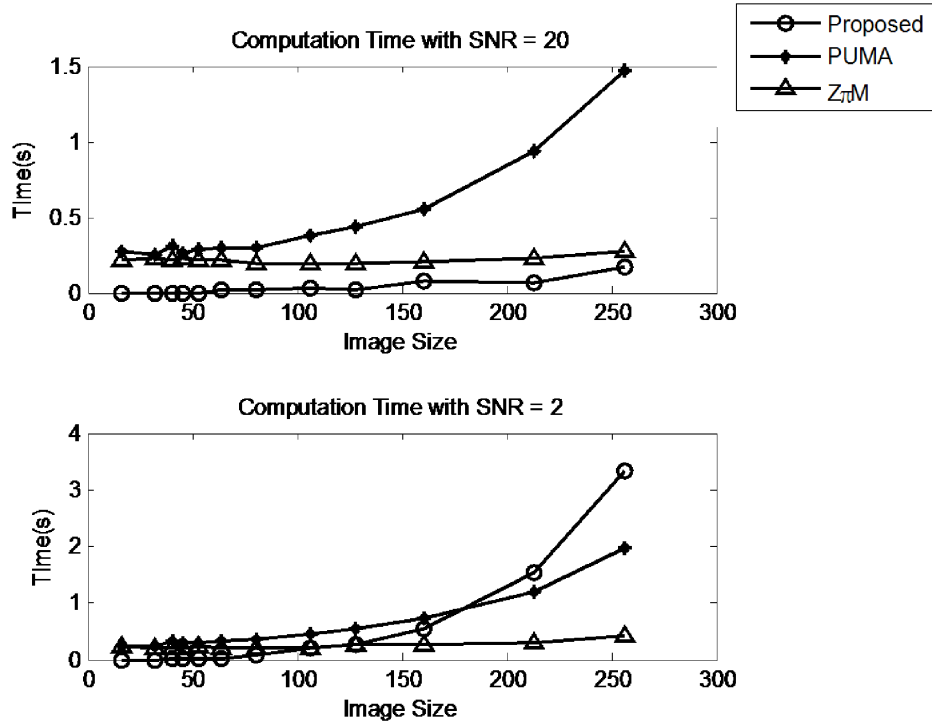


**Fig. 3.8** Computation time for the proposed method, the method in [26], the PUMA method, and the Z $\pi$ M method with SNR ranges from 1.5 to 100.

### 3.4.2 In-vivo MRI brain images

The proposed method was also tested using a set of in-vivo MRI brain images of a healthy male volunteer. The MR image was acquired using fast 3D fast spin-echo sequence and an 8-channel receive-only head coil with the subject staying in a supine position. The data acquisition parameters are: data matrix 256 x 256, TR = 2000 ms, TE = 8.5 ms, length of echoes = 16, number of slices = 32, FOV = 20 x 20 cm<sup>2</sup>, slice thickness = 4 mm, RF receiver bandwidth = 32 kHz, and no data averaging.

The original phase image and unwrapped result by the proposed method are shown in Fig. 3.9 (a) and (b), respectively. The same image was also unwrapped by the method in [26], the PUMA method and the  $Z\pi M$  method. The results are shown in Fig. 3.9 (c), (d) and (e), respectively. The PUMA method performed well when the background noise exists, but an abrupt  $2\pi$  jump exists in the unwrapped phase image. The method in [26] and the  $Z\pi M$  method provided comparable results for this image. However, the unwrapped phase in gray matter in these images are not as uniform as the one from the proposed method. The reason is that the phase in gray matter is affected by some phase jumps close to  $\pi$  in the neighboring regions such as the skull and the white matter. A slightly over  $\pi$  difference may be recognized as a phase wrapping and a slightly under  $\pi$  difference as smooth. If the phase unwrapping methods cannot handle this well, it will result in  $2\pi$  jump in a smooth region. The proposed method is superior in addressing this regard.

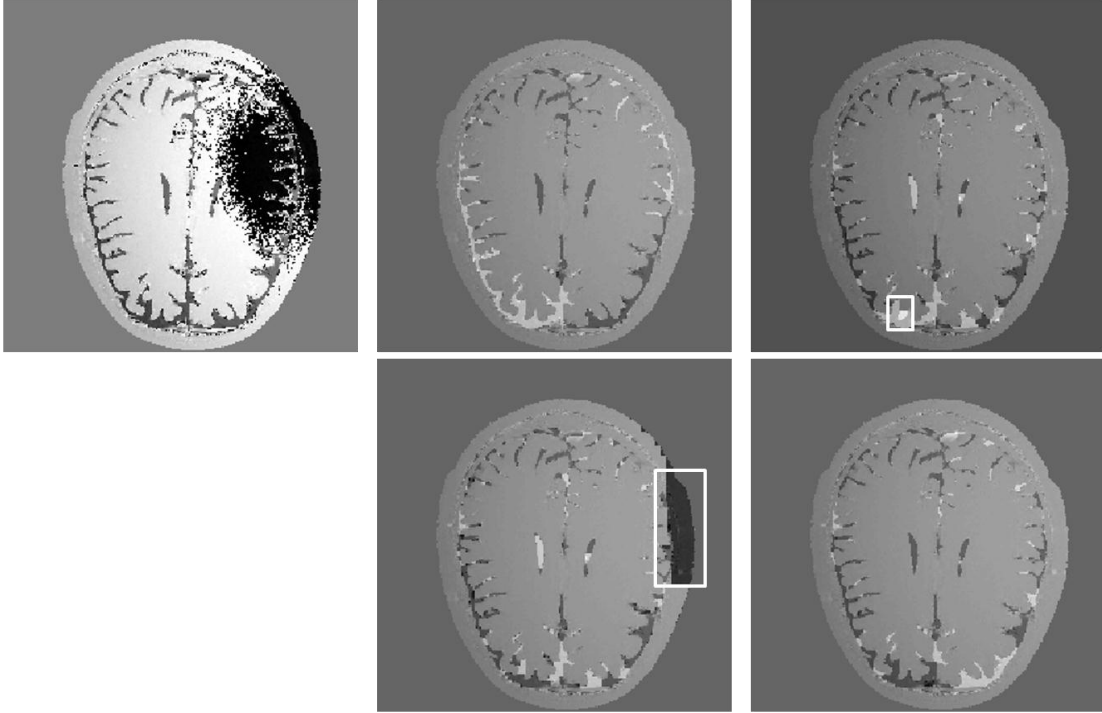


**Fig. 3.9 Phase unwrapping an in-vivo brain MRI image: (a) original phase image; (b) unwrapping phase image by the proposed method; (c) unwrapping phase image by the method in [26]; (d) unwrapping phase image by the PUMA method; and (e) unwrapping phase image by the  $Z\pi M$  method.**

### ***3.4.3 Phase image with cutline***

The four methods are also tested on another MRI data set. The data was acquired using a 3D fast spin-echo sequence with a 180-degree inversion recovery prepulse. All parameters are the same as previous data set except the setting of inversion time  $TI = 450$  ms. The image is shown in Fig. 3.10 (a), and the unwrapped results are shown in Fig. 3.10 (c - f) for the proposed method, the method in [26], the PUMA method, and the

Z $\pi$ M method, respectively. Fig. 3.10 (a) represents a typical problem in phase unwrapping: the image violates the smoothness condition, as mentioned in the introduction. The white arrow points to a region where phase is gradually increasing from up-left to downright direction. The black arrow points to a region where phase is gradually decreasing. The hatched arrow points to the boundary of the phase jump. This represents a very challenging scenario for phase unwrapping. The image shown in Fig. 3.10 (a) can be simplified as the disk in Fig. 3.10 (b). The phase increases clockwise and phase wraps at the right middle region. This could be due to some rapid phase change at some areas in between. As a result, it does not have an exact solution for phase unwrapping. If the phase is treated in a voxel-by-voxel fashion, it may result in endless iterations. However the proposed method seeks for an optimum solution and locates phase jump at some boundary of region, which is more acceptable.

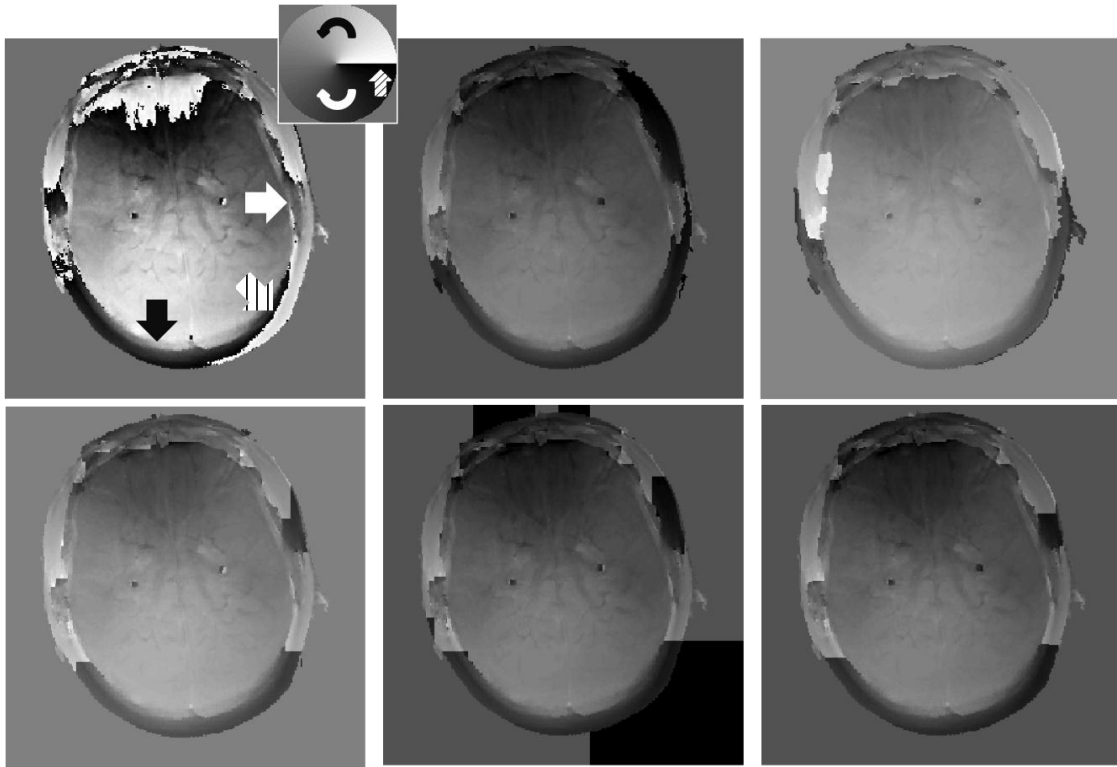


**Fig. 3.10 Phase wrapping an image that violates the smoothness constraint: (a) original phase image; the image contains regions that are challenging to unwrap (see text) as pointed by the arrows, (b) inset illustrating the problem in (a). There is no correct solution as the phase unwrapping will result differently if it follows a clockwise path or a counterclockwise path. The unwrapped phase image shown in (c-g) is from the proposed method, the pole-guided-cutline method, the method in [26], the PUMA method, and the  $Z\pi M$  method, respectively.**

### ***3.4.4 Phase unwrapping for interventional devices***

The proposed method is also applied to the interventional devices, as shown in Fig. 3.11. Though interventional devices introduce fast dephasing in conventional MRI images, the spin-echo sequence with a shifted  $180^\circ$  pulse reduces phase wrapping around the interventional devices by using a small shifted time. Thus, the proposed phase unwrapping method can unwrapped the phase image with minor error, thus obtain relatively accurate field maps.

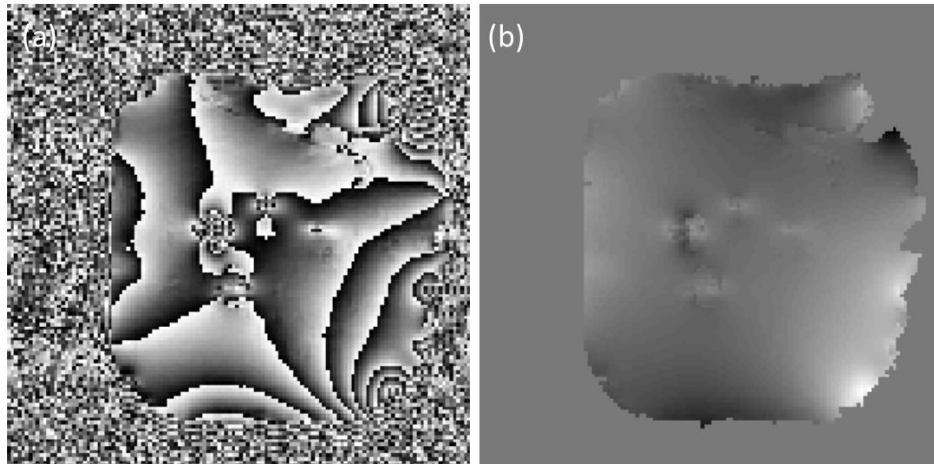


**Fig. 3.11 Phase unwrapping of brachytherapy seeds. (a) The wrapped phase; (b) the unwrapped phase using the proposed method.**

### **3.5 Discussions**

Highest-confidence-first is a local optimization method for MRF. Though a global minimization is preferred, there is no known efficient algorithm available. In reality, one is always facing one of two choices: (1) to find the exact global minimum

with possibly intolerable computation expense or (2) to find some approximations with much less cost [31]. The methods for local minimization are quite mature, thus in this proposed method, a local optimization, instead of a global one, is chosen to perform the phase unwrapping.

The aim to segment phase image into regions is to avoid unnecessary calculation within smooth region. For traditional pixel-based phase unwrapping methods, the number of cliques for one pixel is four in 2D images or six in 3D images. With the arbitrary regions, how robust the proposed method can introduce to the phase unwrapping depends on the complexity of the image. The number of cliques for one region could be one, or larger than 6. For the proposed method, update of the stability is needed every time a label is confirmed. For very noisy images, the number of the segmented regions may be large, which will increase the computation expense. Therefore, more advanced segmentation algorithms might be needed in such scenario.

Another factor that impacts computation efficiency is that once a region is committed, all its neighbors need to update stability and sort. The cost function in the proposed method is the summation of square of neighboring difference, which is proportional to the number of neighboring pixels. So does the stability. Therefore, the neighboring region with more adjacent pixels and less close values may be chosen as the next one to get committed. A parallel version of HCF could decrease the computation time.

The proposed method is programmed in C language and compiled in Matlab, as the method in [26], the PUMA and  $Z\pi M$  methods do. The computation time of the

proposed method is regarded as comparable to that of the other three methods, but acceptable to our experiments since it only takes within a second.

The proposed method is demonstrated using simulated and in-vivo MRI images, but it is expected to be effective for other phase unwrapping appliances as well. The future work is to test other possible potential function, to extend this method to 3D and to implant it on parallel computations plat forms.

### **3.6 Conclusions**

A novel phase unwrapping method based on a region-based Markov Random Field model was presented. The method segments the phase image into regions, and phase unwrapping is performed between regions using a highest-confidence-first method. Results on simulated and experimental MRI images showed that this method provides similar or improved phase unwrapping than the method in [26], Phase Unwrapping MAx-flow/min-cut (PUMA) method and  $Z\pi$ M method. The proposed method is expected to be useful for other phase unwrapping applications.



## CHAPTER IV

### LOCALIZATION OF BRACHYTHERAPY SEEDS IN MRI BY MAPPING THE SUSCEPTIBILITY\*

#### **4.1 Introduction**

##### ***4.1.1 Difficulty in localization of brachytherapy seeds***

Brachytherapy eliminates malignant cancer cells by inserting radioactive seeds directly into the tumor as a localized treatment. For biocompatibility, the shell of the seeds is normally made of titanium, which has a magnetic susceptibility of 182 ppm. Imaging plays a significant role in brachytherapy, including locating the tumor, serving as guidance during seed insertion, and providing post-surgery evaluation. Ultrasound and CT are routinely used for these purposes because of their speed and relatively low cost.

In recent years, MRI has been explored as a new imaging tool in brachytherapy, due to its superior image quality and soft-tissue contrast. As early as the 1980's, MRI has been used to plan the treatment of brachytherapy [35-37]. In 2000, brachytherapy was conducted on 43 patients with prostate cancer using an open MRI, and a larger coverage of the tumor volume was cured by the treatment [38]. In 2004, ten prostate brachytherapy surgeries were conducted with the assistance of MRI in every stage of the procedure and documented in detail [39]. This demonstrates the feasibility and

---

\*Reprinted with permission from "Susceptibility-Based Positive Contrast MRI of Brachytherapy Seeds" by Ying Dong, Zheng Chang, Guoxi Xie, Gregory Whitehead, and Jim X. Ji, 2014. *Magnetic Resonance in Medicine*, Copyright [2014] by Wiley Periodicals, Inc..

superiority of using MRI as the guidance imaging modality. In 2006, combined X-ray and MRI were applied to clinical research in another group, showing an improved localization and differentiation when compared to Ultrasound or CT [40]. MRI can also be used for dosimetric evaluation, which requires the knowledge of the locations and distribution of the implanted seeds relative to the organs and cancer volume.

Nevertheless, the high susceptibility of the metallic shell of the brachytherapy seeds introduces severe signal loss around the seeds on conventional MR images. The equivalent susceptibility of the whole brachytherapy seed (shell + radioactive core) is about 50 ppm, which can increase the magnetic field variation and result in faster dephasing of the spins around the seeds [6]. Therefore, the signals from the nearby tissues decay much faster than those from other areas, thus introducing black holes in and around the seeds. These can be seen from the literature on brachytherapy applications and studies to simulate and validate the image artifacts of the brachytherapy seeds [39-43].

#### ***4.1.2 Related work to provide positive contrast***

As a result of these artifacts, it is sometimes difficult to differentiate the seeds from other dark features in the MRI magnitude image, such as arteries (excited blood flow moves out of the field of view) or natural cavities [7]. Many efforts have been made to create the positive-contrast MR images to improve the visualization of the seeds in MRI. For example, a new pulse sequence, Inversion-Recovery with ON-resonant water suppression (IRON), employs a spectrally-selective on-resonant saturation prepulse to provide positive contrast of the off-resonance tissue areas [2]. Recently, a center-out

Radial Sampling with Off-resonance Reception (co-RASOR) method was proposed to provide positive contrast for small paramagnetic objects by shifting the signal toward the object's center using off-resonance reception [1]. Later on, an improved version of co-RASOR was proposed that uses a single acquisition and off-resonance reception [8]. Co-RASOR methods generally require the knowledge of an appropriate susceptibility value to correctly shift the off-resonance signals to the location of the object. All above methods require significant alternation of pulse sequences, and they may not be straightforward to implement on clinical scanners. In addition, several post-processing methods have been developed to address this problem. One method achieves positive contrast by thresholding the high-pass filtered phase image, though it is only used for cellular imaging [9]. In the Susceptibility Gradient Mapping (SGM) method, the local susceptibility gradient is calculated using a Short-Term Fourier Transform (STFT) over a small window, which is then used to selectively turn the negative contrast into a positive contrast [3]. This method reduces the spatial resolution because the susceptibility gradient is assumed to be constant over the window width. An improved version of SGM, named SGM Using the Original resolution (SUMO), uses a truncated filter in k-space instead of STFT so that the original resolution is maintained [4]. Though the above methods can provide positive contrast of the metallic shells, they are based on the phase of field perturbation due to the seeds, which spread out from the seeds themselves. As a result, the positive contrast regions from these methods extend to much larger areas than the seed itself, which can potentially cause localization errors or misinterpretations.

In this chapter, a new method to generate susceptibility-based positive contrast MRI for visualizing brachytherapy seeds and highlight the seeds at their exact location is proposed. This method directly maps the susceptibility, an inherent property of the seeds. Due to the high susceptibility values and physical size of the seeds, existing Quantitative Susceptibility Mapping (QSM) methods that were developed mostly for Super Paramagnetic Iron Oxide (SPIO) or naturally occurring iron-induced susceptibility cannot be straightforwardly applied to this problem [10, 44-47]. In this chapter, a method that uses equivalent ultra-short TE spin-echo sequences and an improved susceptibility mapping technique is presented for this application. An appealing aspect of the method is that signals from the surrounding areas are used to derive the susceptibility of the seeds where signal magnitude is low. Specifically, a unique weighting matrix and a masking matrix are applied to overcome the low SNR and low data fidelity due to the rapid signal decay around the seeds. Numerical simulations and phantom experiments show that the proposed method provides positive contrast for the seeds at the exact seed locations, thereby demonstrating its benefits compared to the existing methods. The research is based on the preliminary work reported at a conference [48].

## **4.2 Theory**

Modeling of the magnetic field due to a known susceptibility distribution in an external magnetic field has been extensively studied in the literature. Various methods have also been proposed to measure the susceptibility using MRI [10, 45, 46].

Specifically, the magnetic field due to an object of arbitrary shape can be modeled as the convolution of its susceptibility distribution with the dipole kernel [44, 46, 49, 50]:

$$\Delta\mathbf{B}(\mathbf{r}) = \boldsymbol{\kappa}(\mathbf{r}) \otimes \boldsymbol{\chi}(\mathbf{r}) \quad (4.1)$$

where  $\Delta\mathbf{B}(\mathbf{r})$  is the field map with respect to  $B_0$ , i.e.  $\Delta\mathbf{B}(\mathbf{r}) = (\mathbf{B}(\mathbf{r}) - B_0)/B_0$ ,  $\boldsymbol{\kappa}(\mathbf{r})$  is the dipole kernel, and  $\boldsymbol{\chi}(\mathbf{r})$  is the susceptibility distribution, which can be derived from the measured  $\Delta\mathbf{B}(\mathbf{r})$  by a deconvolution. The direct way to calculate  $\boldsymbol{\chi}$  using Fourier domain deconvolution is known to be difficult due to the singularity and ill conditions [51]. Methods to address this problem, including the one in this chapter, often rely on numerical regularization. Interested readers are referred to [44-46]. Mostly related to the work presented here is the regularized  $L_1$  method presented in [46], where  $L_1$  minimization is used to regularize the solution of the inverse problem of Eq. 4.1. Anatomical information is used to define a masking matrix to further improve the solution.

A notable feature of existing susceptibility mapping methods is that a relatively long echo-time, e.g. 5~20ms, is usually used. Such echo-times are optimized for applications where susceptibility due to SPIO or naturally occurring iron is to be mapped. When they are directly applied to the brachytherapy seed imaged by MRI, severe signal loss in the regions near the seeds occur, making it necessary to use very large regularization, which can compromise the integrity of the solution.

### 4.3 Methods

The proposed method consists of two major components: (I) a data acquisition scheme that allows field mapping of areas near high susceptible seeds, where signals are subject to severe  $T_2^*$  decay; and (II) an improved sparsity-driven regularization framework that makes it possible to derive the susceptibility distribution of the seeds themselves, even though the signals in the immediate vicinity of the seeds are almost completely lost.

#### 4.3.1 Data acquisition using SE sequence with shifted $180^\circ$ pulse

A Spin-Echo (SE) sequence with shifted  $180^\circ$  pulse is used in the proposed method to acquire the data. SE sequences yield data with higher SNR and minimal distortion when compared to many Gradient Echo (GE) pulse sequences. More importantly, SE sequences allow the collection of phase information with equivalent ultra-short echo shifts. Instead of being in the center of the echo time, the  $180^\circ$  pulse is shifted by  $T_{shift}$ , which can be very short and is defined as positive if it is shifted towards the excitation pulse [52-54]. The susceptibility-induced phase only accumulates for  $2T_{shift}$  instead of the entire TE.

#### 4.3.2 Susceptibility mapping with regularized $L_1$ minimization

The mathematical framework is similar to the method presented in [46, 55, 56], which is based on the regularized  $L_1$  minimization, where  $\chi$  in Eq. 4.1 is obtained by

$$\arg \min_{\chi, \lambda} f(\chi, \lambda) = \|\mathbf{W}(\mathbf{C}\chi - \Delta\mathbf{B})\|_2^2 + \lambda \|\mathbf{M}\mathbf{G}\chi\|_1 \quad (4.2)$$

where  $\mathbf{W}$  is a weighting matrix,  $\lambda$  is a regularization parameter,  $\mathbf{M}$  is a masking matrix, and  $\mathbf{G}$  is a first order gradient operator to promote sparsity. Here,  $\mathbf{W}$  is calculated by normalizing the magnitude image. This is based on the assumption that low signal will yield low SNR, and thus low reliability. Because of very high seed susceptibility, data in the immediate vicinity of the seeds contains little useful information. With low magnitude and rapid phase wrapping, the phase information is not reliable. Therefore, a weighting matrix is used to lower the weight of the unreliable information around the seed for the data consistency term.

Though similar formulation has been proposed in [46, 55, 56], the rationale and the definition of  $\mathbf{M}$  in the proposed method are different. In [46],  $\mathbf{M}$  is defined based on the assumption that edges in the magnitude image and in the susceptibility map should generally appear in the same locations if homogeneous regions in the magnitude image also have homogeneous susceptibility. The small size and high susceptibility of the seeds necessitate affect the definition of  $\mathbf{M}$ . Specifically, mask  $\mathbf{M}$  is defined to exclude all areas that may contain highly susceptible objects and their vicinities, which avoids over-smoothing in these areas. At the meantime, it also allows the regularization to provide artifact removal and denoising at the pixels far from the seeds. Mask  $\mathbf{M}$  is derived by thresholding the magnitude image. The magnitude of signals from the susceptible objects and its surrounding tissues is low, and the mask will exclude them from the regularization term in Eq. 4.2. In this work, the threshold is experimentally set to be 20% of the maximum voxel magnitude. It is noteworthy that the mask  $\mathbf{M}$  does not need to exactly match with seed locations. It could be larger or smaller than the seeds, or at a

location with no seed inside. Unlike other QSM techniques, the proposed method does not require an accurate calculation of seed and surrounding tissue susceptibility to produce an image. Therefore,  $\lambda$  can be chosen from a relatively large range without affecting the performance. Note that  $\boldsymbol{\chi}$  in Eq. 4.1 is defined over the whole field of view, including the areas where  $\mathbf{M}=0$ .

Solution to Eq. 4.2 is obtained by first setting the first-order derivative to 0,

$$\frac{\partial f}{\partial \boldsymbol{\chi}} = 2\mathbf{C}^H \mathbf{W}^H (\mathbf{W}(\mathbf{C}\boldsymbol{\chi} - \Delta\mathbf{B})) + \lambda \nabla \|\mathbf{M}\mathbf{G}\boldsymbol{\chi}\| = 0 \quad (4.3)$$

where  $^H$  is the conjugate transpose of the operator/matrix. The  $L_1$  norm is not continuous at  $\mathbf{M}\mathbf{G}\boldsymbol{\chi} = 0$ . Therefore, a small regularization number is added to make it continuous, and thus differentiable [57]. The approximation of Eq. 4.3 becomes

$$\frac{\partial f}{\partial \boldsymbol{\chi}} \approx 2\mathbf{C}^H \mathbf{W}^H (\mathbf{W}(\mathbf{C}\boldsymbol{\chi} - \Delta\mathbf{B})) + \lambda \mathbf{G}^H \mathbf{M}^H \mathbf{T}^{-1} \mathbf{M}\mathbf{G}\boldsymbol{\chi} \quad (4.4)$$

where  $\mathbf{T}$  is a diagonal matrix with  $t_k = \sqrt{(\mathbf{M}\mathbf{G}\boldsymbol{\chi})_k^* (\mathbf{M}\mathbf{G}\boldsymbol{\chi})_k + \mu}$  as the diagonal elements, where  $\mu$  is a small positive number, experimentally set to  $10^{-15}$ . Then Eq. 4.4 is solved iteratively using a nonlinear conjugate gradient method [57]. The introduction of  $\mu$  makes  $\mathbf{T}$  positive definite, therefore the solution converges within a finite number of iterations. The iteration stops either when the gradient is smaller than a preset threshold or when the maximum number of iterations is reached.

### ***4.3.3 Computer simulations***

To evaluate the performance of the proposed method, synthetic MRI data with a known susceptibility map were generated using computer simulations and then



processed using the proposed method. Images with different seeds orientation and spacing, spatial resolution and noise levels were simulated. To simulate the images, a high-resolution susceptibility map was first constructed according to the structure of the brachytherapy seeds. The structure of the seeds is very delicate, with multiple layers that are several micrometers thick, as shown in Fig. 4.1a [58]. To achieve accurate simulation, the susceptibility of all materials in a voxel was calculated by taking a weighted average according to the fractional volumes. The field map was then calculated by convolving the susceptibility map with the dipole kernel. Subsequently, the images were simulated based on their spin densities. The echo time shift,  $T_{shift}$  was set to be 0 and 0.3ms, respectively, for the two acquisitions. In the simulation, the seeds were placed either parallel or perpendicular to the  $B_0$  field, which corresponds to the closed and open bore MRI, respectively. Note that no prior knowledge about seeds orientation is required for the proposed method to work. Gaussian noises yielding different SNR were also added to both the real and imaginary part of the images.

A sequence of images at several resolutions were calculated based on the highest resolution images simulated at a resolution of 50um in x and y directions, and 0.15mm in z direction. The FOV is  $5.12 \times 5.12 \times 1.05 \text{ cm}^3$ , producing an image size is  $1024 \times 1024 \times 70$ . Three seeds were placed with a spacing of 5mm and 10mm in the first simulation. And one seed was placed at [2.25cm, 2.25cm] in the FOV in the second and third simulation. The lower resolution images (0.5 mm, 1mm, and 1.5mm in-plane resolution) were simulated by subsampling the high-resolution images.

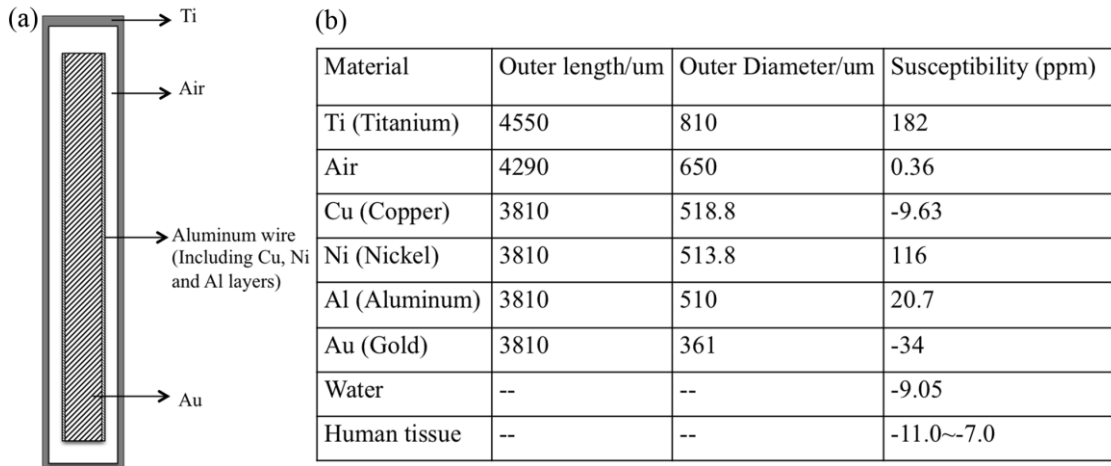


**Fig. 4.1 (a) The structure of a dummy STM 1251 I-125 brachytherapy seed; (b) The dimension and susceptibility of the materials in the seed [6].**

#### **4.3.4 Experimental data acquisition**

To further test the proposed method, three sets of experimental data were acquired on a 33cm-core 4.7T Varian scanner. The first dataset was acquired using a gelatin phantom with which the brachytherapy seeds location is straightforwardly controlled. The phantom was built using the following procedure: (I) the gelatin solution was doped with copper sulfate to reduce the  $T_1$  and  $T_2$  relaxation time; (II) part of the solution was poured into a MR-compatible container and rested for concretion; (III) two STM 1251 I-125 dummy seeds were placed on top; (IV) then the rest of the gelatin was filled in and rested for concretion. The phantom was imaged using a birdcage coil, with the seeds being parallel to the magnetic field. A multi-slice spin-echo sequence was used to acquire the axial slice data, with echo shifts of  $T_{shift} = 0.3\text{ms}$  and  $T_{shift} = 0\text{ms}$ . The

acquisition parameters are: matrix size =  $128 \times 128 \times 7$ ; FOV =  $80 \times 80 \times 10.5\text{mm}^3$ ; slice thickness = 1mm, slice gap = 0.5mm; TR = 2s, and TE = 30ms. The field map was calculated voxel-by-voxel according to

$$\Delta\mathbf{B} = \frac{\Delta\theta}{2\gamma B_0 \Delta T_{\text{shift}}} \quad (4.5)$$

where  $\theta$  is the phase of the image voxel.

In the second experiment, a needle was used to insert three brachytherapy seeds into pork meat (see Fig. 4.7(a)), which mimics human biological tissue. Additionally, a plastic stick was inserted to simulate a natural void, and a bamboo toothpick was inserted to simulate a capillary. The seeds in this experiment were placed perpendicular to the  $B_0$  field. Image slices were acquired in the sagittal plane, which was perpendicular to the longitudinal direction of the seed. The experimental data were acquired using the same parameters as those used in the first experiment.

In the third experiment, 6 brachytherapy seeds with different spacing (5mm, 11mm, and 15mm) were inserted into pork meat (see Fig. 4.8(a)) to study the limitation of the proposed method. The seeds orientation and imaging parameters were the same as the second experiment, except the slice thickness was set to 1.5mm with no gap.

All k-space data were transferred to a computer with the Mac OS X operation system, 2.5 GHz Intel Core i5, 4GB 1600MHz DDR3 memory. Data processing was performed in Matlab 7.11.0 (R2010B, MathWorks, Natick, MA).

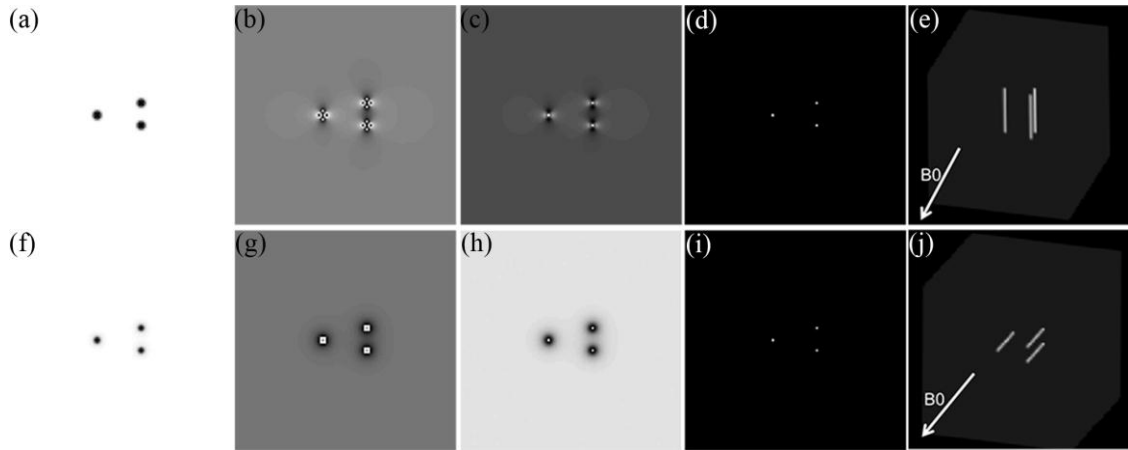
After reconstructions, a measurement called half-intensity region is calculated for each simulation and experimental data set. The half-intensity region is defined as the

number of pixels that differ from the background tissue by at least  $\frac{1}{2}(I_{\max} - I_{\min})$ , where  $I_{\max}$  and  $I_{\min}$  are the maximum and minimum intensity of the pixels in the area. This measure shows the point-spread reduction between seeds in ordinary negative-contrast magnitude images and those in susceptibility-based positive contrast images.

## 4.4 Results

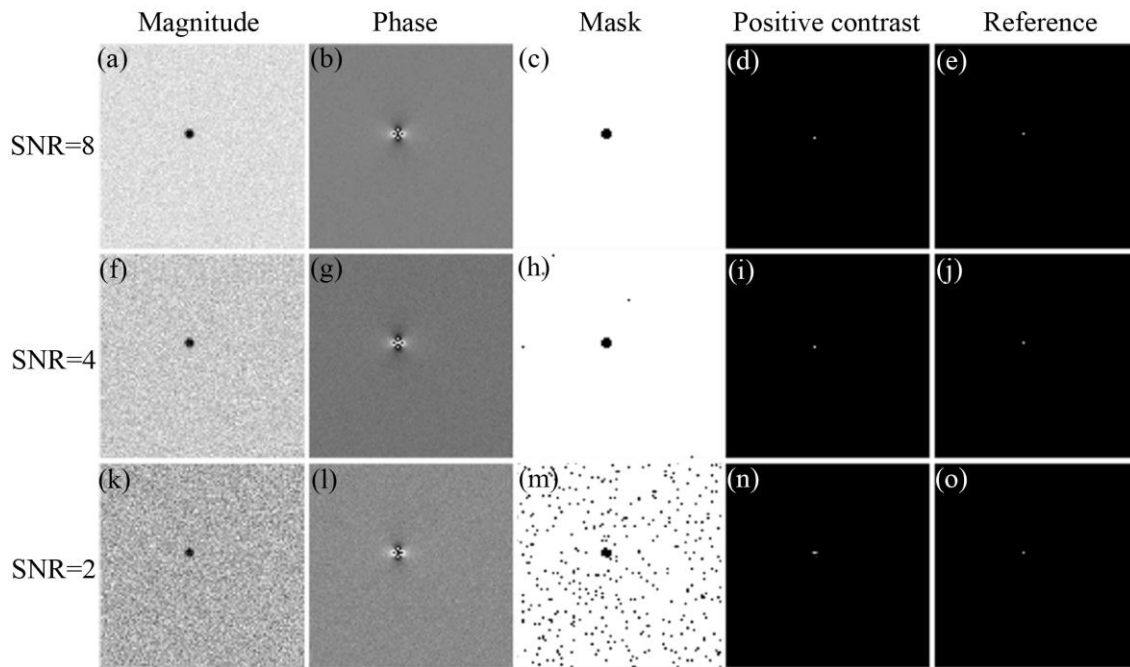
### 4.4.1 Computer simulations

Fig. 4.2(a) shows the result from the first computer simulations. The top row corresponds to seeds placed perpendicular to the static magnetic field, and the bottom row corresponds to seeds placed parallel to the field. As shown in Fig. 4.2(a),(f), seeds appear as dark spots, each of which occupies an area of about 13 pixels, which is much larger than the physical size of a single seed ( $\sim 0.8$  mm in diameter, or 1 pixel). Fig. 4.2(b),(g) depict the phase images, and Fig. 4.2(c),(h) show the calculated field maps. Using the proposed method, the seeds can be clearly identified and localized, since each one occupies only a single pixel in both Fig. 4.2(d) and Fig. 4.2(i). The Maximum Intensity Projection (MIP) renderings of the susceptibility map are shown in Fig. 4.2(e),(j). The locations and the size of the seeds are clearly shown in the reconstruction. Note that although the orientation of the seeds differs, the proposed method was able to correctly visualize and locate the seeds in both cases.



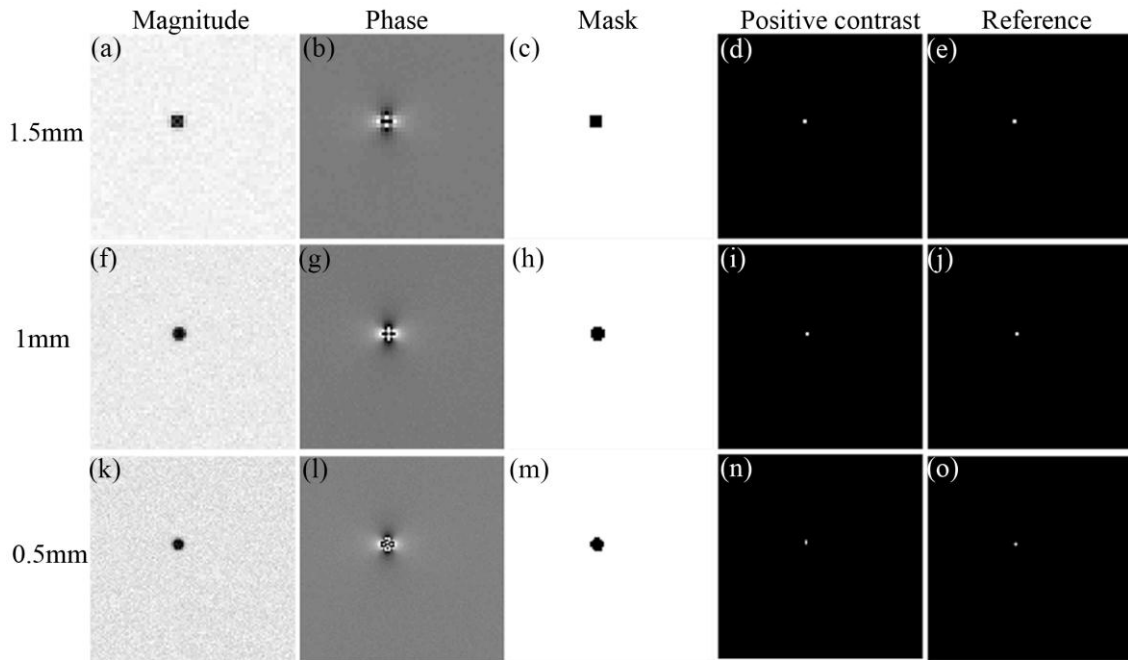
**Fig. 4.2 The simulated images (representative slice) and the corresponding results using the proposed method from the slices perpendicular to the seeds: (top row) seeds perpendicular to  $B_0$ , (bottom row) seeds parallel to  $B_0$ ; (a)(f) magnitude image, (b)(g) phase image, (c)(h) field map, (d)(i) susceptibility map calculated by the proposed method, and (e)(j) maximum intensity projection rendering of susceptibility maps.**

Fig. 4.3 shows the results where different levels of noise were added to the data. The proposed method performed as expected in all three cases. Even when there is significant noise on the mask covering many “false” areas (as in the cases of SNR = 4 and 2), the proposed method still provided accurate location of the seeds. However, with very noisy data (such as when SNR = 2), the results from the proposed method started to deteriorate, and positive contrast was shown in an enlarged area.



**Fig. 4.3 Reconstructions of a seed at different SNR in the simulated studies: (first row) SNR = 8, (second row) SNR = 4 and (third row) SNR = 2; (a) (f) (k) magnitude images, (b) (g) (l) phase images, (c) (h) (m) mask generated by thresholding the magnitude images, (d) (i) (n) positive contrast images from the proposed method, and (e) (j) (o) reference of the true seed location.**

The effect of the proposed method with respect to different resolutions was also studied, the results of which appear in Fig. 4.4. This study shows the proposed method can correctly localize the seeds using a range of resolutions, making it more practical for clinical applications.



**Fig. 4.4 Reconstruction of a seed with images simulated at different resolutions: (first row) 1.5mm, (second row) 1mm, and (third row) 0.5mm; (a) (f) (k) magnitude images, (b) (g) (l) phase images, (c) (h) (m) masks, (d) (i) (n) positive contrast images created using the proposed method, and (e) (j) (o) reference of the true seed image location.**

#### **4.4.2 Experiments with tissue phantoms**

Figs. 4.5-4.6 demonstrate experimental results with a gelatin phantom in which the seeds were placed parallel to the static magnetic field, resulting in a round pattern around the seeds on the axial images. Fig. 4.5(a) shows the magnitude image of the center slice. As expected, the seeds and their neighboring pixels are shown as dark spots, each occupying about 8 pixels. Fig. 4.5(b) is the phase image with  $T_{shift} = 0.3\text{ms}$ , and Fig.

4.5(c) shows the calculated field map, which clearly depicts the effect of the strong susceptibility on the neighboring pixels. Finally, the positive-contrast susceptibility images of the seeds using the proposed method are shown in Fig. 4.5(d). The images of the seeds are much narrower and closer to their physical size than those depicted in Figs. 4.5(a),(c). It is worth noting that the shadings that appear over the entire field of view of the images shown in Figs. 4.5-4.6 are likely due to  $B_0$  field inhomogeneity or from the induced field from the geometry of the phantom, as no shimming was performed during the data acquisition and no background phase removal was performed during data processing.

The proposed method was compared to the SUMO method [4], and a representative result is shown in Fig. 4.6. As shown in Fig. 4.6(a), whereas the proposed method produced a positive contrast image of the seeds at their locations, SUMO generated highlighted “rings” surrounding the seeds, which are much larger than the physical profiles of the seeds themselves (see Fig. 4.6(b)). A one-dimensional cross-section that intersects one seed appears in Fig. 4.6(c) and provides additional evidence to support this observation. The MIP reconstructions of the two results are shown in Fig. 4.6(d),(e). Clearly, the 3D reconstruction using the proposed method provides a more accurate rendering of the seeds, and therefore more precise seed localization, than the MIP reconstruction generated using the SUMO technique.



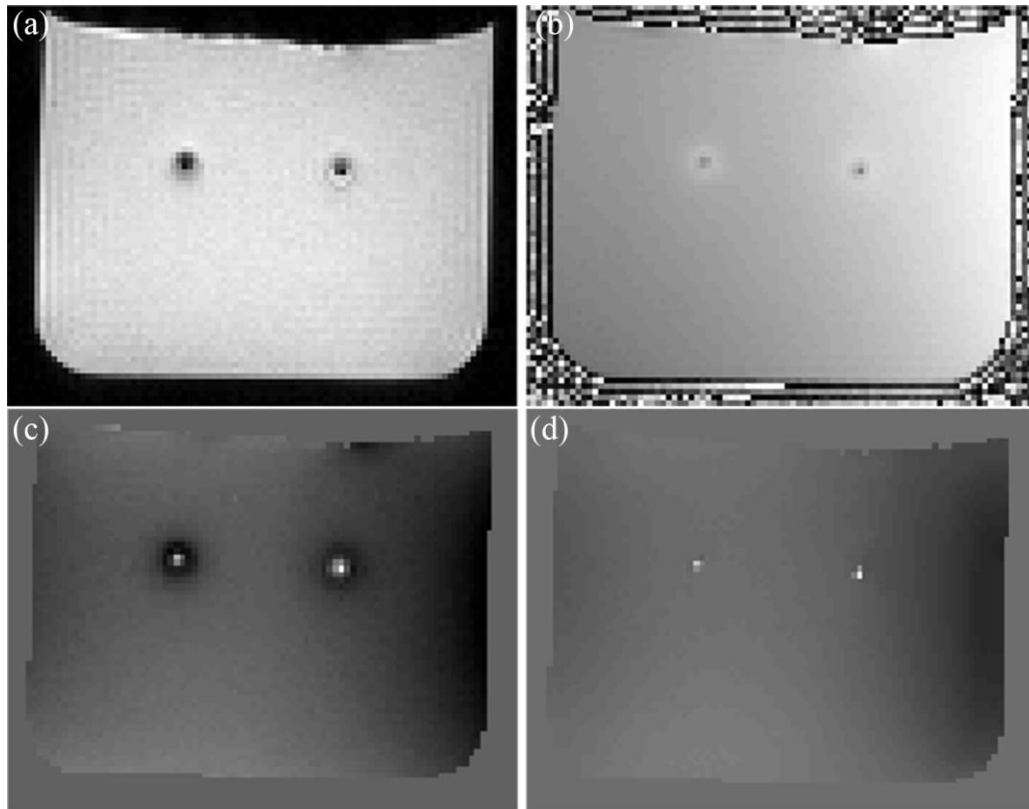


**Fig. 4.5** A representative axial slice reconstructed from a gelatin phantom with two dummy seeds: (a) magnitude image from the spin echo acquisition, (b) phase image from the acquisition with  $T_{shift} = 0.3\text{ms}$ , (c) calculated field map, (d) positive contrast image using the proposed method.

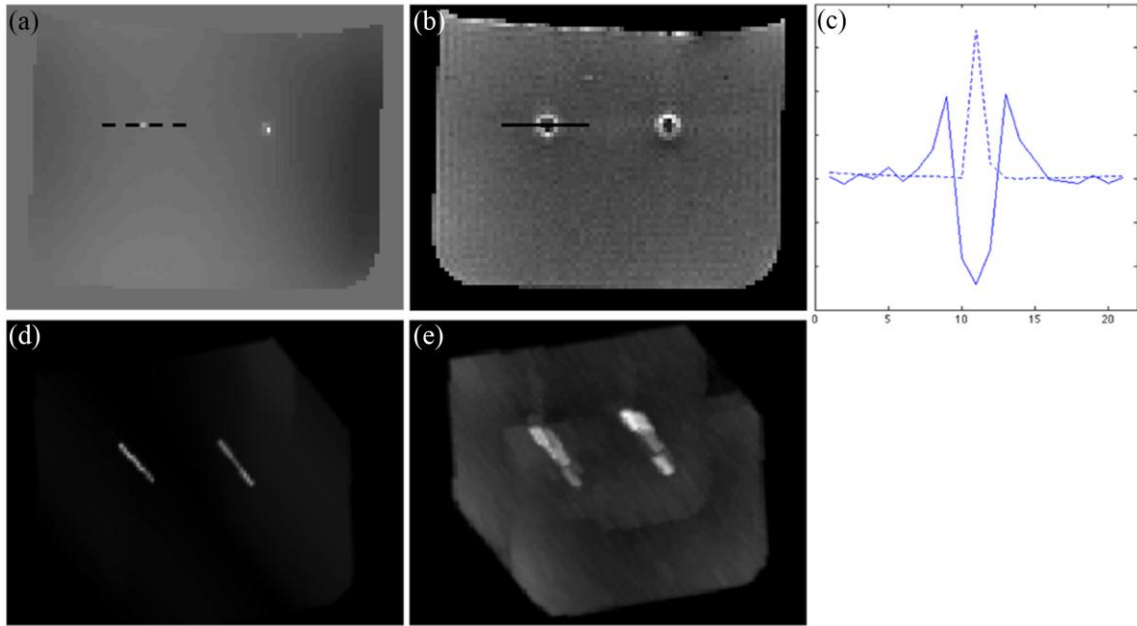


**Fig. 4.6** The positive contrast images created by (a) the proposed method, and (b) the SUMO method; (c): zoomed-in 1D cross-section near the left seed, indicated by the line segments in (a) and (b); (d) MIP reconstruction from the 3D reconstruction by the proposed method; (e) MIP reconstruction from images processed by the SUMO method.

Images and comparisons on a representative slice of the 3D dataset in the second phantom experiment are shown in Figs. 4.7. Fig. 4.7(a) is a photo of the tissue phantom, and Fig. 4.7(b) is the magnitude image of the center slice. The lower green arrow indicates the position of the plastic stick, and the upper red arrow indicates the position of the bamboo toothpick. Interestingly, small regions around the three seeds show some signal enhancement due to the distortion at  $T_{shift}$ . However, up to 25 pixels ( $\sim 10\text{mm}^2$ )

around each seed are shown as dark spots. Fig. 4.7(c),(d) show the phase images for  $T_{shift} = 0\text{ms}$  and  $0.3\text{ ms}$ , respectively. When  $T_{shift} = 0\text{ms}$ , there are no significant phase variations due to  $\Delta B$  around the brachytherapy seeds because of the  $180^\circ$  refocusing pulse, as expected. Phase at the exact seed locations is due primarily to noise. At  $T_{shift} = 0.3\text{ ms}$ , significant phase variations can be clearly seen in Fig. 4.7(d), particularly around the seeds. In this experiment, the seeds were perpendicular to the static magnetic field, resulting in a spindle pattern around the seeds. One can see that from the magnitude and the phase images, it is hard to differentiate the seeds from the two voids induced by the plastic and bamboo sticks.

Fig. 4.7(e) shows the field map calculated from the phase images. Although obvious differences between the seeds and other structures can be seen, the locations of the seeds are not precisely defined. However, Fig. 4.7(g) demonstrates substantial differences between the seeds and other structures using the proposed method, and, the seeds are visualized with improved definition and accuracy. The number of pixels per seed has been reduced from around 25 pixels in Fig. 4.7(b) to 3 pixels in Fig. 4.7(g), which is closer to the physical seed size. Note that the size of the seeds is also much smaller than the mask depicted in Fig. 4.7(f), which verifies that the proposed method does not critically depend on the accuracy of the mask to work. Fig. 4.7(h) shows the positive contrast image created using the SUMO method. Again, it is observed that the proposed method reconstructed the seed faithfully at the accurate location, while the more straightforward SUMO method highlighted the surrounding tissues.

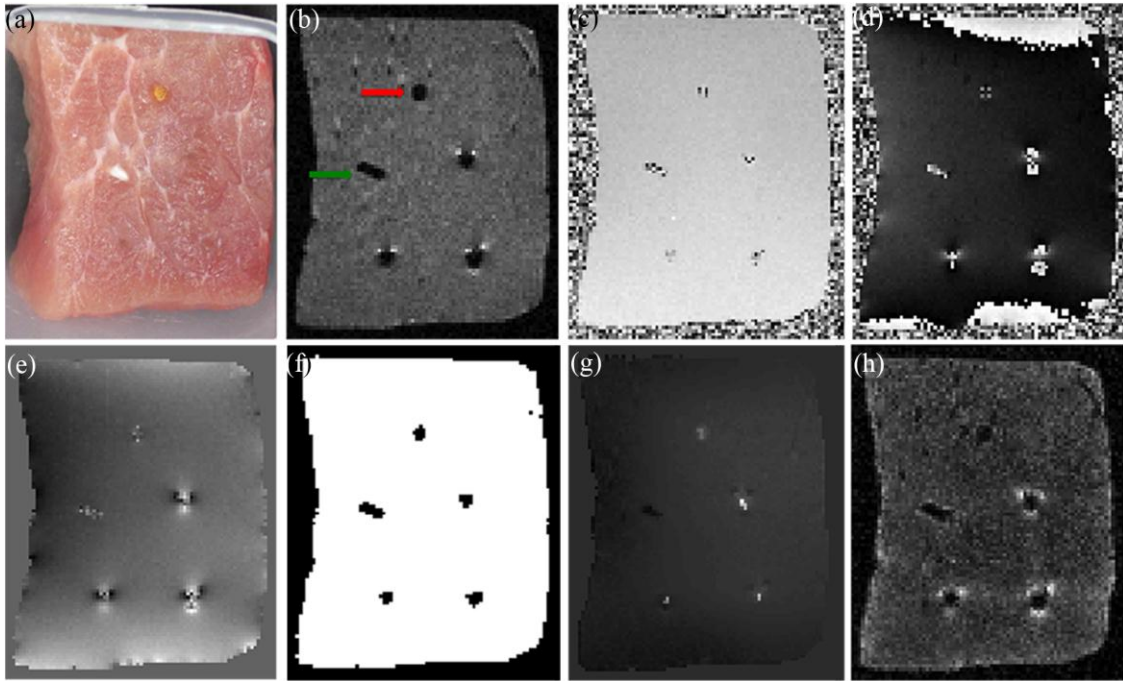


**Fig. 4.7 Upper row: Images from the first tissue phantom experiment: (a) photo of the phantom; (b) magnitude image; (c) phase image with  $T_{shift} = 0$  ms; and (d) phase image with  $T_{shift} = 0.3$ ms. As shown, in addition to the three seeds, a bamboo toothpick (upper red arrow) is used to simulate capillary and a plastic stick (lower green arrow) is used to simulate natural cavities and voids. Lower row: Reconstructions using two different methods: (e) calculated field map; (f) mask  $M$ ; and (g) positive contrast image generated by the proposed method, and (h) by the SUMO method. Note that seeds are placed in the phantom such that they are perpendicular to the  $B_0$  field.**

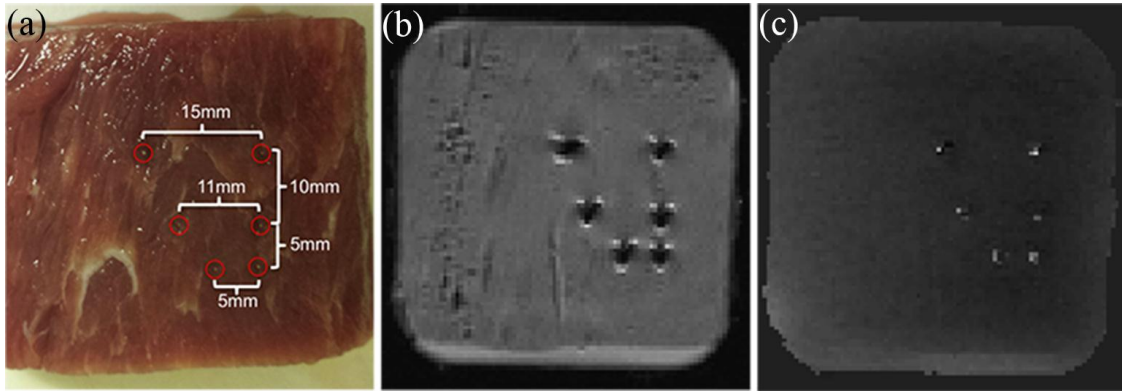


**Fig. 4.8 Images from the second tissue phantom experiment: (a) photo of the phantom with the spacing between the seeds labeled; (b) magnitude image; and (c) positive contrast image generated by the proposed method.**

Images and comparisons on a representative slice of the 3D dataset in the third phantom experiment are shown in Figs. 4.8. Fig. 4.8(a) is a photo of the tissue phantom where the locations and the spacing between the seeds are labeled. Fig. 4.8(b) shows the magnitude image of the center slice. The susceptibility map calculated by the proposed method is shown in Fig. 4.8(c). The results demonstrate the proposed method can correctly locate the seeds as close as 5mm, which is the smallest spacing in most clinical settings.

Table 4-1 lists the half-intensity regions from the magnitude images and the images reconstructed using the proposed method. The percentage reductions of the half-intensity regions in different experiments are also listed on the right column. As shown, in most cases, the proposed method reduced the point spreading by more than 70%. The

half-intensity regions in the positive contrast images are much closer to the real size of the seeds. This gain significantly improves the visualization of seeds.

*Table 4-1 The half-intensity regions and reduction rates in the computer simulations and phantom experiments. Data from representative slices shown in Figs. 4.2~4.8*

		Magnitude images	Positive contrast Images	Reduction rate
Simulation 1	Perpendicular	21	1	95%
	Parallel	13	1	92%
Simulation 2	SNR=8	21	1	95%
	SNR=4	21	1	95%
	SNR=2	22~24	7	68%~71%
Simulation 3	Res=1.5mm	9	1	89%
	Res=1mm	21	1	95%
	Res=0.5mm	33	1	97%
Gelatin phantom with 2 seeds		5~8	1~2	75%~80%
Meat phantom with 3 seeds		19~25	2~4	84%~89%
Meat phantom with 6 seeds		13~21	1~4	69%~95%

## 4.5 Discussions

The susceptibility of interventional devices is known to cause dark spots in MR images. The previously presented results have demonstrated that the proposed method can inversely compute the susceptibility distribution. Thus the proposed method addresses this problem by producing images with devices shown in positive contrast, since they exhibit higher magnetic susceptibility than typical biological tissues. In this research, the effectiveness of this method has been established using phantom experiments with dummy brachytherapy seeds. Future work will extend the application of the proposed method to imaging larger devices, such as stents and biopsy needles.

The SUMO method demonstrates its ability to provide positive contrast images in tissues surrounding the brachytherapy seeds in literature. But it does not show good contrast using the spin-echo sequence in this work. One potential reason is the shifted echo time that we used was too small. The TE used in [4] for brachytherapy seeds is 4.6ms, whereas the effective TE used in this research is only 0.6 ms.

The susceptibility images obtained from the proposed method can be straightforwardly combined with the conventional images, so both soft tissues and the seeds can be visualized concurrently [9]. By doing so, both good soft-tissue contrast and accurate brachytherapy seed localization can be achieved simultaneously.

In order for the susceptibility mapping to work, the proposed method must use images acquired by multiple slices with sufficient resolution, while other existing methods such as SUMO can be applied to a single slice. It should be noted, however,

that practical MRI visualization and localization of brachytherapy seeds requires multiple-slice 3D images due to the small size of the seeds.

Due to the large susceptibility, the field gradient close to a seed could potentially affect the slice selection profile. However, the maximal susceptibility-induced field distortion drops to 5ppm at about 1.5 mm from the center of the seeds. As the signals within the immediate vicinity of the seeds has very low magnitude due to dephasing, they will not likely to introduce large distortion to slice profile. Moreover, a 3D spin echo sequence can be used to alleviate the non-uniform excitation. However, it requires long acquisition time, which may reduce its utility in clinical applications.

The simulation and experimental results show that the proposed method can differentiate the seeds with a reasonable distance. Additional experimental data, though not presented in the chapter, show that the proposed method can differentiate the seeds with a distance greater than 3mm. Since the typical spacing of the brachytherapy seeds is about 1cm, the proposed method is capable of differentiating the adjacent seeds in clinical applications [59].

The proposed method is limited in several aspects. First, due to the small size of the brachytherapy seeds and partial volume effect, the calculated susceptibility is in general lower than the theoretical prediction. This is due in part to the fact that the structure of the seeds is very complex, with multiple layers of different material inside. However, in most cases, only the average susceptibility of all materials in the voxel (titanium, aluminum, air and biological tissues) will be reflected. It is interesting to point out that lower quantified susceptibility values have been reported in [60] for a simple



sphere structure. Furthermore, computed susceptibility also depends on the size of the voxel. There is a critical resolution below which there will be insufficient spatial sampling of the field, and the proposed method may fail. The proposed method also requires longer reconstruction time than conventional MRI or the other more straightforward methods like SUMO. In the experiments presented in this chapter, it took between 3 to 10 seconds to reconstruct one 3D image using Matlab. Last but not least, the proposed method relies on signals with sufficient SNR from the surrounding areas of the seeds to calculate the image phase and susceptibility (even though the SNR can be extremely low at the immediate vicinity of the seeds). This is why the observed seeds diameters in Table 1 are larger than the expected values. Nevertheless, the objective of this study is to provide improved visualization and identification of the brachytherapy seeds, and the results presented herein demonstrate that the proposed method is very promising for this application.

#### **4.6 Conclusions**

In this chapter, a new method based on susceptibility mapping to provide positive contrast MRI visualization of brachytherapy seeds was presented. Both simulated and experimental phantom data were used to test the proposed method with different image resolutions and seed orientations. The results show that the proposed method can provide positive contrast for the seeds and correctly differentiate the seeds from other structures that appear similar to the seeds on conventional magnitude images.

## CHAPTER V

### LOCALIZATION OF LARGE-SIZE INTERVENTIONAL DEVICES AND SPEEDUP

In this chapter, we extend the method in Chapter IV to other larger interventional devices. Furthermore, we combined the method with compressive sensing because the acquisition time using spin-echo sequence with a shifted  $180^\circ$  pulse is long. An improved reconstruction method using compressive sensing with composite sparsifying transforms is also presented.

#### **5.1 Localization of Other Interventional Devices with Larger Size**

##### ***5.1.1 Introduction of larger interventional devices***

Certain interventional procedures, such as brachytherapy, biopsy and angioplasty, can be monitored using MRI if the devices used are MRI compatible. However, the objects, such as needles, markers, stents, and brachytherapy seeds, still have one-order higher magnetic susceptibility than human tissue. The high-susceptibility objects will affect their surrounding area and introduce fast dephasing thus decrease the signal-to-noise ratio (SNR). A dark hole and bright dots due to signal shifting appear and cover an area of several times larger than the devices itself in the MR images [2, 39]. This artifact hinders the accuracy of the localization of the devices, and prevents MRI from being widely used in these procedures.

There are several methods that address this problem. The susceptibility gradient mapping using the original resolution (SUMO) method is a post processing method that

calculates the gradient of the susceptibility using a truncation filter in the k-space. At the boundary of the susceptible objects, the gradient is large. Therefore, SUMO method provides positive contrast image of the contour of the susceptible objects. A shortcoming of the SUMO method is that it depends on the phase variation, which will be a little larger than the actually size of the susceptible objects.

To accurately locate the brachytherapy seeds, our group has previously proposed a method based on susceptibility mapping to provide the positive contrast seed images [61]. In the method, susceptibility is calculated by deconvoluting the magnetic field map with a dipole kernel. In this application, the devices are small (on the order of voxel size). However, with biopsy or angioplasty, the biopsy needles or stents have a much larger physical size and more severe signal loss. Susceptibility mapping of these devices has not been demonstrated due to the signal void or low SNR at or near the device locations.

Common methods to localize and provide positive-contrast of these devices includes shifting the surrounding data to the location of the devices [8], mapping the susceptibility gradient by selectively turn the negative contrast into a positive contrast using a filter or short-term Fourier transform [3, 4]. However, these methods depend on pre-knowledge of the susceptibility of the devices and provide limited resolution.

Our previous method, creating positive contrast images using susceptibility mapping, requires spin-echo sequence with shifted 180 pulse. However, this pulse sequence is time-consuming, especially we need multiple (at least 2) acquisition with different shifting time. Compressive sensing is a rapid developing method to reduce acquisition time. Though it is usually used to reconstruct the magnitude image with a

small amount of k-space data, we found out the reconstructed phase image is acceptable for our purposes, because generating positive contrast images and identifying the location of interventional devices doesn't require high quantitative accuracy.

In this paper, we extend our previous method, creating positive contrast images for brachytherapy seeds, to other highly susceptible objects. We first utilize the full k-space data to test whether our previous method is capable for larger devices. We then applied the compressive sensing reconstruction with composite sparsifying transform to our method to reduce acquisition time. To test the proposed method, a gelatin phantom with a piece of platinum wire (susceptibility  $\sim 279$ ppm) and a water phantom with a titanium (susceptibility  $\sim 182$ ppm) biomarker needle are imaged. The corresponding positive contrast images are generated using 1) full k-space data, and 2) reduced k-space data [6]. Results show that the proposed method can provide much improved visualization of devices in positive contrast and help to achieve better devices localization.

### ***5.1.2 Data simulations and experimental acquisitions with full-k-space data***

Two highly susceptible objects were imaged using a 4.7T Varian 33cm scanner. In the first experiment, a platinum wire was placed in a gelatin phantom. A spin-echo sequence with a shifted  $180^\circ$  RF pulse was applied. The matrix size was  $128 \times 128 \times 9$ . The FOV was  $70 \times 70 \text{mm}^2$ . The slice thickness was 1.5mm without slice gap. The TR was 2s, and the TE was 30ms. Six sets of images were acquired, with  $180^\circ$  RF pulse being shifted by  $T_{shift} = [0, 0.1, 0.2, 0.3, 0.4, 0.5]$ ms respectively. Phase unwrapping was applied on the phase images. Two selected sets of data were used to calculate the field

map, according to  $\Delta\mathbf{B} = \frac{-\Delta\phi}{2\gamma B_0 \Delta T_{shift}}$ , where  $\Delta\phi$  is the phase change after phase unwrapping,

and  $\gamma$  is the gyromagnetic ratio.

A computer simulation was conducted to mimic the experimental setup and explore the accuracy of the susceptibility calculation. A high resolution images with 61um x 61um x 0.17mm resolution and 1152x1152x81 image size were created. Independent Gaussian noise was added to the real part and imaginary part of the data separately. Then the data was summated and averaged to 128x128x9 to simulate the spin-spin interaction. The other parameters were chosen so that they were consistent with the experimental data. The shape of the titanium wire was simplified as a circle.

In the second experiment, a biomarker needle was inserted in to a water phantom, which was doped with 1g/L copper sulfate. The acquisition parameters were the same as the first experiment.

### ***5.1.3 Reconstruction using CS with composite sparsifying transform to reduce acquisition time***

The platinum wire dataset is used for this test. We simulated a radial acquisition with a reduced number of k-space lines using the fully sampled dataset. Totally 40 radial lines each with 128 data points (28% of full k-space data) were extracted to reconstruct the image. Daubechies filter with length 4 and level 1 is used in the proposed method.

Both the deconvolution reconstruction and compressive sensing reconstruction procedures were performed offline using Matlab (Math Works, Natick, MA) and a house-made nonlinear conjugate gradient method. The computer has 2.5GHz Intel Core

i5, 4GB 1600 MHz DDR3 memory and OS X system. Multiple regularization parameters were tested and visually compared to choose the best results.

#### **5.1.4 Reconstruction using full k-space data**

Fig. 5.1 shows the results from the first phantom experiment. Fig. 5.1 (a) shows the gelatin phantom with the platinum wires (more gelatins were later filled on top of the platinum wire). Fig. 5.1 (b) shows a representative magnitude image in the center slice using the spin-echo sequence with a shifted  $180^\circ$  pulse. Because of the high susceptibility of the platinum, the magnitude image shows dark area up to 2.2mm in ring width, comparing with the diameter of the wire of 0.3mm. Fig. 5.1(c) and (d) shows the corresponding phase images when  $T_{shift} = 0\text{ms}$  and  $0.2\text{ms}$ . When  $T_{shift} = 0\text{ms}$ , the phase should be uniform across the phantom. However, the field variation induced by the high susceptibility will affect the excitation pattern. To calculate the field map, different  $\Delta T_{shift}$  are tested.  $\Delta T_{shift} = 0.1\text{ms}$  can provide correct field map, as shown in Fig. 5.1(e). And Fig. 5.1(f) shows the susceptibility map calculated using the proposed method. Comparing to Fig. 5.1(b), the platinum wire shows in positive contrast in Fig. 5.1(f), making it much easier to see and localize.

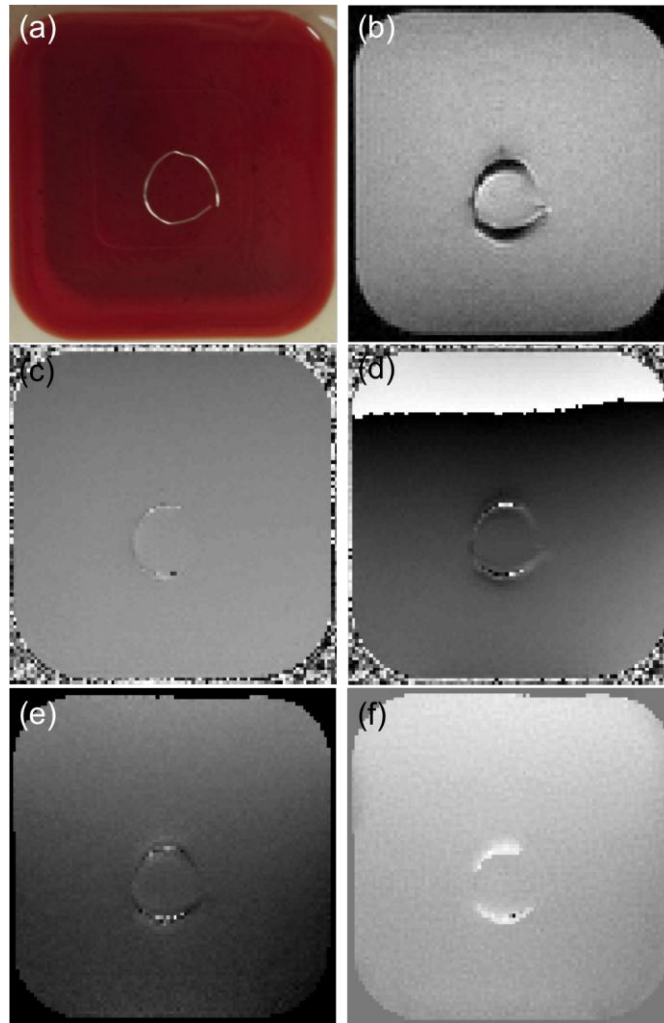


**Fig. 5.1 (a) Photo of the platinum wires in a gelatin phantom; (b) MR magnitude image; (c) phase image with  $T_{shift} = 0ms$ , (d) phase image with  $T_{shift} = 0.2ms$ ; (e) calculated field map; and (f) susceptibility image from the proposed method. The edges of the images are cropped for better visualization.**

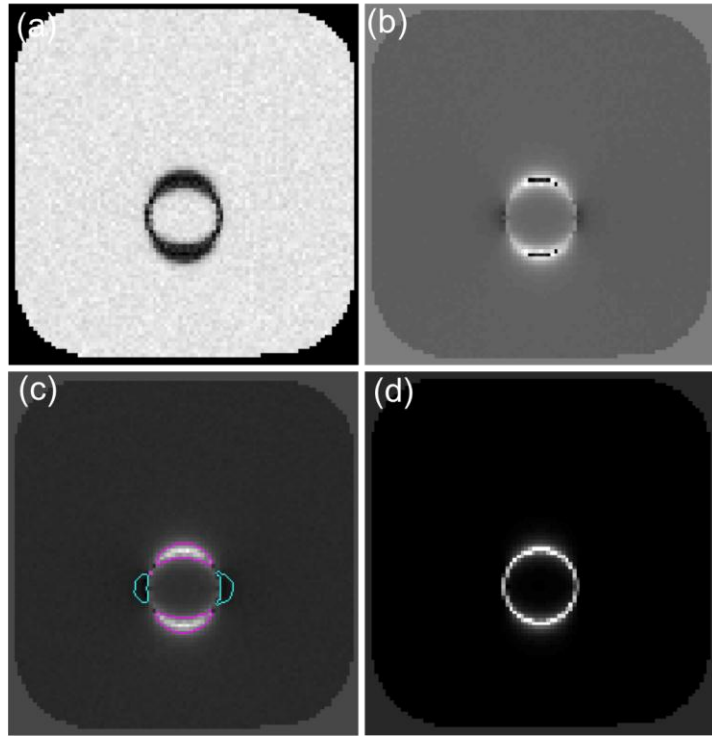


**Fig. 5.2 The results from the computer simulation. (a) Magnitude image; (b) Phase image when  $T_{shift} = 0.2\text{ms}$ ; (c) the ideal field map without noise, with  $\pm 10\text{ppm}$  contour labeled; and (d) the susceptibility map calculated using the proposed method.**

Fig. 5.2 shows the results of the computer simulation. Fig. 5.2(a) and (b) show the magnitude and phase image ( $T_{shift} = 0.2\text{ms}$ ) of the center slice in the simulation. They correspond well to Fig. 5.1(b) and (d). Fig. 5.2(c) shows the field map and the  $\pm 10\text{ppm}$  contour of the field map. Fig. 5.2(d) shows the susceptibility map calculated using the proposed method. The proposed method produced a highly localized, clear representation of the position of the susceptible objects.



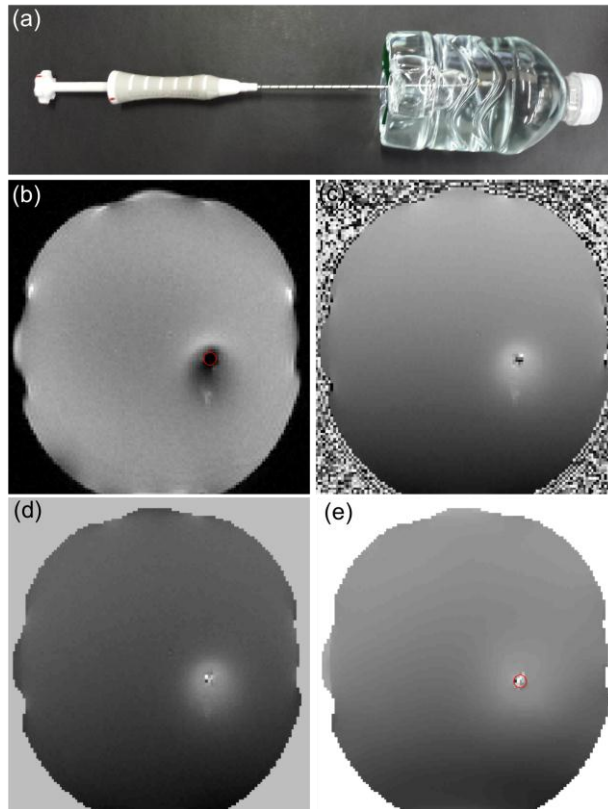


**Fig. 5.3 (a) Photo of the biomarker needle in water phantom; (b) magnitude image; (c) phase image with  $T_{shift} = 0.1\text{ms}$ ; (d) field map calculated from the phase images; and (e) susceptibility map from the proposed method. The edges of the images are cropped for better visualization.**

The results from the second phantom experiment are shown in Fig. 5.3. Fig. 5.3(a) shows a picture of the water phantom for the second experiment. The needle is made of titanium and the size of the needle is 14G (~2mm in diameter). The water is doped with copper sulfate to make the  $T_1$  and  $T_2$  of the water close to the human muscles. Fig. 5.3(b) and (c) shows the magnitude and phase ( $T_{shift} = 0.1\text{ms}$ ) of the spin-

echo sequence with a shifted  $180^\circ$  pulse, respectively. The presence of the needle introduces great distortion to both the magnitude and phase image. Fig. 5.3(d) shows the field map calculated from the phase images. And Fig. 5.3(e) shows the susceptibility map calculated using the proposed method. As shown, the susceptibility map calculated using the proposed method reduces the image artifacts and shows the location in positive contrast.

## **5.2 Image Reconstruction Improvement Using Compressive Sensing with Composite Sparsifying Transforms**

### ***5.2.1 Introduction of compressive sensing***

Compressive sensing (CS) technique can recover a “sparse” image from a substantially reduced number of measurements less than what is dictated by the sampling theorem. In MRI, CS has proven to be an effective approach to reduce the data acquisition time, therefore allows faster imaging [57]. One important condition for the CS technique to work is that the images must have sparse representations in some basis. For images that are sufficiently sparse, restricted isometry property (RIP) condition guarantees the exact reconstruction when there is no noise; or a reconstruction with limited error when the measurements contain noise [62, 63].

Many efforts have been paid to find optimal sparsifying transforms (or sparse representations) to improve CS-MRI. A number of recent works in this area are based on dictionary learning where a dictionary is learned from a training set or iteratively from the measurements. This is a promising technique for CS-MRI that is out of the scope of

this paper. Interested readers are referred to [64, 65]. In this paper, we focus on the sparsity measures or sparse representations that are based on conventional, non-adaptive transforms. These include, but not limited to, first-order finite difference (for Total Variations), wavelet [57, 62], contourlet [66], curvelet [67], discrete cosine transform (DCT) [31], and Laplacian [68]. Each specific representation may be particularly suitable for compressing certain kinds of features, but may have limited sparsifying capability for other features. For example, the finite-difference works well for piece-wise constant features, but may introduce staircase artifact for rapid changing features [69]. Wavelet transform is good for point-like features, but it could introduce some noise-like artifact in the background where no signal is expected. For a comprehensive understanding of diverse transforms, readers are referred to [70]. An important realization since the early literature on CS-MRI is that multiple sparse representation terms can be combined to improve the reconstruction quality [49, 57, 71, 72]. In the literature, the combination is generally performed by a linear summation of the predefined sparse representations. For example, TV and wavelet filters are used and balanced by two regularization parameters in [57]. Plonka proposes curvelet and wavelet transforms (though not specifically for MR images) [73]. Another group tested different transforms and showed that the linear summations can provide improved results [71, 74]. However, using multiple sparsifying transform terms in this way means that each term must be weighted by a regularization parameter. To determine the two (or more) regularization parameters, multiple reconstructions with different choice of parameters need to be performed so the “optimal” set of parameters can be identified. Practically the

L-curve method can be extended to multiple dimensional cases to choose the parameters, but the procedure could be extremely time-consuming [75].

In this paper, a new method is proposed to combine sparsifying transforms for CS-MRI. In this method, two or more sparsifying transforms are cascaded to form a composite transform, i.e. they are applied to an image sequentially. As such, the method can take advantage of both transforms, but only needs to tune a single regularization parameter. This treatment is expected to increase transform sparsity, and in the same time maintain reconstruction quality. Experimental results from both simulated and in-vivo MRI data show that the proposed method yields similar image reconstruction quality, but takes significantly less time than the conventional methods where multiple sparse representations are combined linearly. This paper is developed based on a preliminary report in [61].

### ***5.2.2 Compressive sensing MRI with combined sparsifying transforms***

In MRI, the measurements acquired in the spatial-frequency domain (also known as k-space) are related to the underlying image  $x$  by  $b = Ax$ , where  $b$  is the stacked column vector representing the acquired k-space data,  $A$  is the reduced-rank Discrete Fourier Transform (DFT) matrix, and  $x$  is the stacked column vector representing the image to be reconstructed. In the conventional MRI, the k-space data are sampled according to the Nyquist rate such that  $A$  is full-rank. Image reconstruction is simple by multiplying  $b$  with the inverse of  $A$ , which accounts to the inverse DFT. In CS-MRI, only a subset of k-space data is acquired at “randomized” k-space locations. The image reconstruction can be achieved by solving the following convex optimization problem

$$\begin{aligned} & \arg \min_x \|\Psi x\|_1 \\ & \text{subject to } Ax = b \end{aligned} \quad (5.1)$$

where  $\Psi$  is a sparsifying transform and  $\Psi x$  is the transform coefficients. CS theory requires that the inverse transform of  $\Psi$  to be sufficiently incoherent with  $A$ , i.e., the rows of  $A$  should not have a sparse representation in terms of the columns of  $\Psi$ , and vice versa [76]. Since  $A$  is a reduced-rank DFT matrix that corresponds to the “randomized” k-space locations, a variety of transforms can loosely satisfy this condition in practice.

The problem in Eq. 5.1 is usually addressed by turning it into the unconstrained form

$$\arg \min_x g(x) = \lambda \|\Psi x\|_1 + \|Ax - b\|_2^2 \quad (5.2)$$

where  $\lambda$  is the regularization parameter to balance the first term (sparsity) and the second term (data consistency).

In several papers, it is shown that the combination of two sparsity terms provides improved reconstruction result than a single transform [57, 71]. In doing so, image reconstruction is achieved by solving

$$\arg \min_x f(x) = \lambda_1 \|\Psi_1 x\|_1 + \lambda_2 \|\Psi_2 x\|_1 + \|Ax - b\|_2^2 \quad (5.3)$$

where  $\lambda_1$  and  $\lambda_2$  are two regularization parameters and  $\Psi_1$  and  $\Psi_2$  are two different sparsifying transforms. Optimal selection of the regularization parameters is not discussed in the above literatures, but it is generally agreed that it is an important factor for image reconstruction quality. However, optimizing these parameters is not trivial. In

most cases, multiple trials with different values are performed and the “optimal” one is selected after assessing the corresponding reconstructions.

In this paper, we propose to use a combined sparsifying transform in the following formulation

$$\arg \min_x g(x) = \lambda \|\hat{\Psi}x\|_1 + \|Ax - b\|_2^2 \quad (5.4)$$

where  $\hat{\Psi}$  is a composite transform such that  $\hat{\Psi} = \prod_{i=1}^m \Psi_i$ , where  $\Psi_1, \dots, \Psi_m$  are individual sparsifying transforms, and  $\prod$  indicates the sparsifying transforms will be applied sequentially. To make an effective composite transform, a variety of individual transforms can be chosen according to the general characters of the images to be reconstructed. Due to the computation associated with composite transform, normally we limit  $m$  to two or three.

Eq. 5.4 can be solved using a nonlinear conjugate gradient method. As shown in [57]

$$\nabla g(x) = 2A^H(Ax - b) + \lambda \nabla \|\hat{\Psi}x\|_1 \quad (5.5)$$

where  $^H$  denotes the Hermitian conjugate. Since  $\|\hat{\Psi}x\|_1$  is not differentiable at 0, a small number is added to make it differentiable. As a result, Eq. 5.5 can be approximated by

$$\nabla g(x) \approx 2A^H(Ax - b) + \lambda \hat{\Psi}^H W^{-1} \hat{\Psi}x \quad (5.6)$$

where  $\hat{\Psi}^H = \prod_{i=1}^m \Psi_i^H$ , and  $W$  is a diagonal matrix with the diagonal elements

$\omega_k = \sqrt{(\hat{\Psi}x)_k^* (\hat{\Psi}x)_k + \nu}$  where  $\nu$  is a very small positive number to avoid singularity. In

this paper,  $\nu$  is set to  $10^{-15}$ . The matrix  $W$  is positive definite, therefore the conjugate gradient is guaranteed to converge within a finite number of iterations. Note that in the proposed formulation, only one regularization parameter,  $\lambda$ , needs to be tuned. This makes it more efficient to solve (5.4) than to solve (5.3) where two parameters need to be tuned.

One key component in the proposed method is the composite sparsifying transform. Many sparsifying transforms have been used for CS-MRI, such as curvelet, wavelet and finite-differences. The sparsifying transforms should be selected according to the feature of the image. Finite difference is capable of constant-like feature, wavelet is capable of point-like feature, and curvelet is capable of line-like feature [77-79]. Another criterion to choose the sparsifying transform is that it should be incoherent with sampling matrix  $A$ .

### ***5.2.3 Data preparation and performance evaluation***

Three sets of k-space data are used to test the methods. For each dataset, we simulated a radial acquisition with a reduced number of k-space lines using the fully sampled dataset. Reconstructions using the proposed method are compared with the conventional methods (wavelet, TV, or the linear summation of the two terms) on both image quality and reconstruction time. In these test, the composite transform consists of cascaded combined finite-differences (TV) and wavelets.

The first dataset was acquired during a breast exam on a 1.5 T clinical scanner. The data was acquired with a 3D fast gradient echo sequence. The k-space data from one slice was used to test the algorithms. Acquisition data matrix is 128 by 128 from which

totally 40 radial lines each with 128 data points (28% of full k-space data) were extracted to reconstruct the image. Daubechies filter with length 4 and level 1 is used in conventional CS method with wavelet transform and the proposed method.

The second is a brain image dataset that was acquired from a healthy volunteer using a fast spin-echo (FSE) sequence on a 1.5T clinical scanner. The data matrix size 256 by 256. The method to extract undersampled radial k-space lines is the same as the first data set. Totally 70 radial lines (25% of full k-space data) were used to reconstruct the image. The filter for conventional CS with wavelet transform and the proposed method is the same as the first data set.

The third data set is an abdomen image. The dataset was acquired using a 3 Tesla clinical scanner with Dual Echo T1-weighted sequence. The matrix size is 512 by 512. Slice thickness is 6mm, repetition time is 230ms, and echo time is 5.8ms. 138 radial lines (25%) are sampled.

To assess the reconstruction quality, three complex images reconstructed from the fully sampled k-space data are used as reference (shown in Fig. 5.4 (a-c)). Specifically, the normalized mean square errors (NMSE) of a reconstructed image is

defined as  $\frac{\|I_r - I_o\|_2^2}{\|I_o\|_2^2}$ , where  $I_r$  is the reconstructed image and  $I_o$  is the reference image.



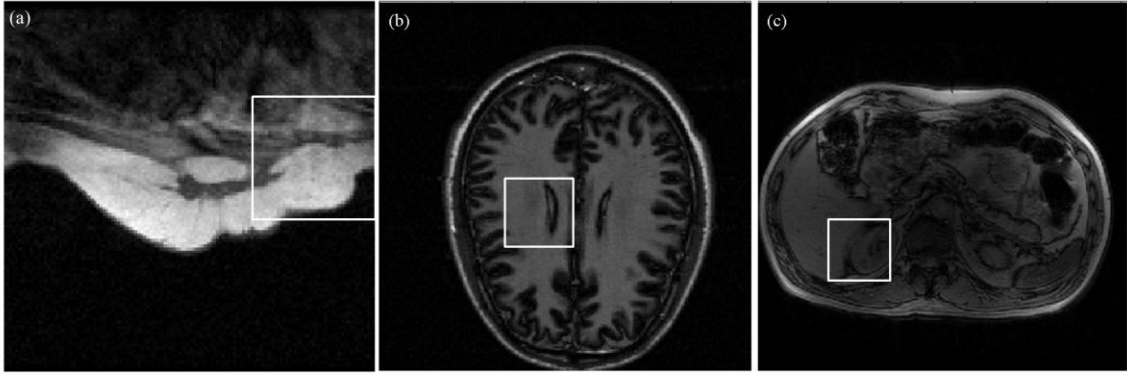


**Fig. 5.4** The reference images reconstructed from the fully sampled k-space data. **(a) breast MRI, (b) brain image, and (c) abdominal image. Details inside the regions highlighted in rectangular boxes are shown in Figs. 5.7 and 5.8.**

To find the optimal reconstruction using four methods, multiple regularization parameters are tested and the best results for each method are selected by visually comparison. The L-curves are also generated, which serve as a guide to choose the best reconstruction. A typical L-curve for single regularization term and linear summation is shown in Fig. 5.5. Specifically, the computational time to find the optimal solution with different  $\lambda$  and NMSE of the reconstructed image are calculated. The computational time is the total time to reconstruct the images using eight regularization parameters, i.e.  $\lambda = [1, 0.1, 0.02, 0.01, 0.001, 0.0001, 0.00001, 0.000001]$ . For the linear summation problem, both regularization parameters are chosen from this set. Therefore, it requires 64 reconstructions, comparing to 8 for the other three methods.

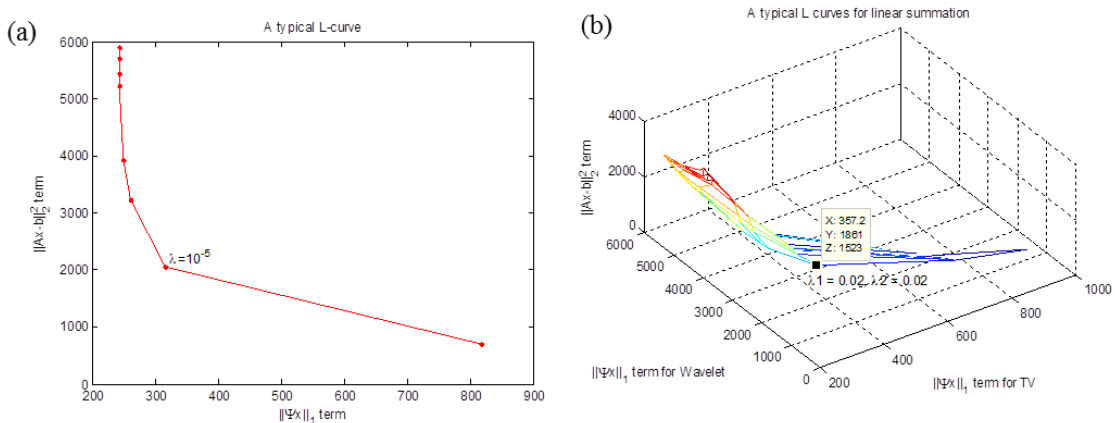


**Fig. 5.5 A typical L-curve for (a) single regularization term and (b) linear summation of two regularization terms.**

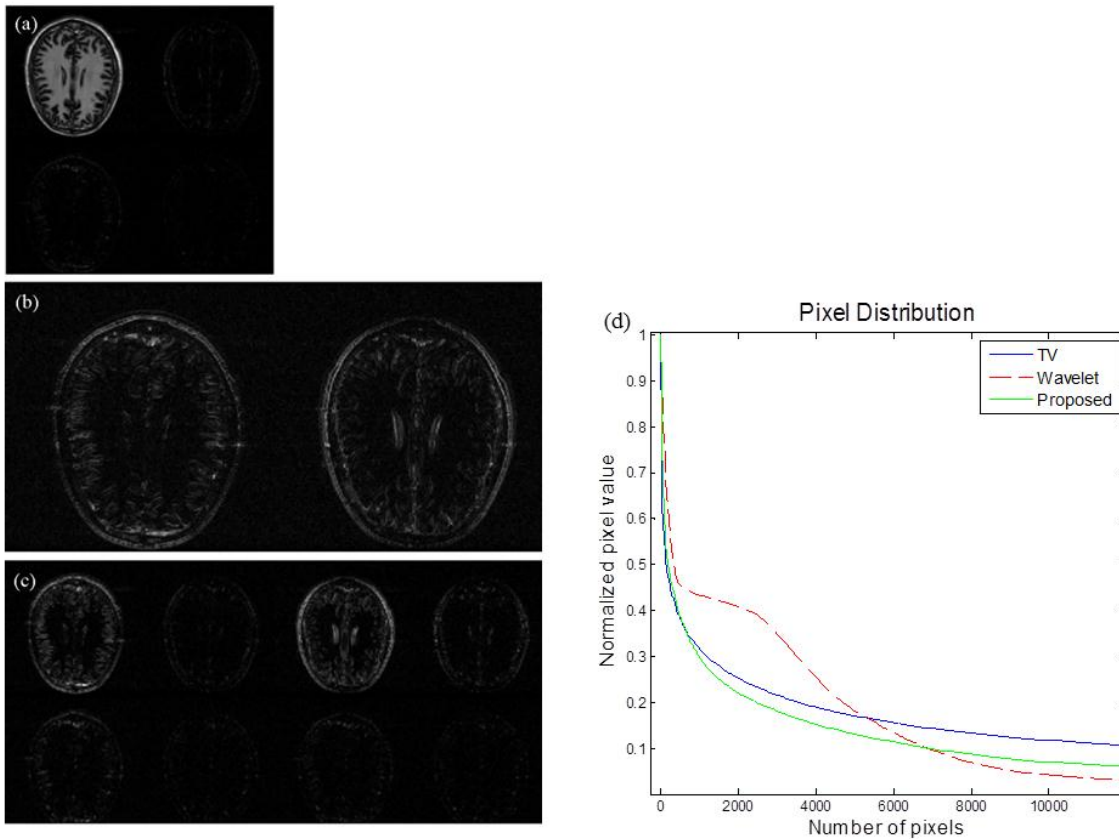
To avoid the bias introduced by visualization, one can also use the SNR as a guidance to select the best reconstruction. Other quantitative parameters, such as signal-to-error ratio, or NMSE requires the reference images, which may not be available in the real compressive sensing acquisition and reconstruction.

This CS reconstruction procedure was performed offline using MATLAB (Math Works, Natick, MA). The wavelet transform is calculated using Wavelab [80]. The nonlinear conjugate gradient method is developed in house based on SparseMRI [57]. The processor of the computer is Intel® Core™ 2 Duo CPU T8300 @2.40GHz, the RAM is 2GB, and the system is Windows 7 Ultimate.

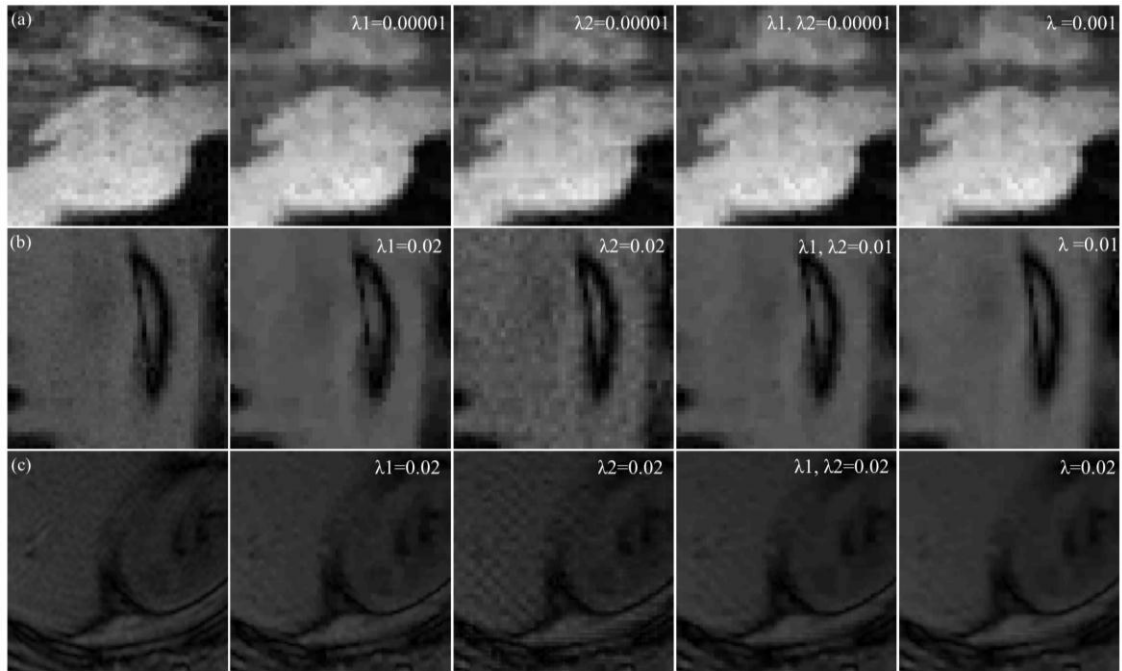
### 5.2.4 Results

Fig. 5.6 illustrates the transformed brain image with different sparsifying transform. The wavelet transform used in (a) and (c) is Daubechies with length 4 and

level 1. As shown in Fig. 5.6 (d), the composite (TV and wavelet) transform results in less number of significant pixels. This means that the proposed method provides highest transform sparsity, therefore an improved reconstruction can be expected.



**Fig. 5.6 Sparsifying transforms applied to the brain image: (a) wavelet transform, (b) finite-differences, (c) composite (wavelet and finite-difference) transform of second data set (real and imaginary), and (d) pixel distribution of the three transforms, which shows that the proposed composite transform yields improved sparsity.**



**Fig. 5.7 CS reconstructions of the highlighted regions in Fig. 5.4 of: (a) breast image; (b) brain image; and (c) abdominal image. Different columns show (from left to right): reference images, reconstructions using TV, Wavelet, linear summation of TV and Wavelet, and the proposed method (last column). On each reconstruction,  $\lambda_1$  is the weight for TV term,  $\lambda_2$  is the weight for wavelet, and  $\lambda$  is the weight for the proposed method.**

Fig. 5.7 shows the CS reconstructions from the three datasets using TV (finite difference), wavelet, linear summation of the two, and the proposed composite transform as sparsifying transforms. Regions highlighted in Fig. 5.4 are zoomed in so that the details can be better visualized. As can be observed, images reconstructed using TV has staircase artifact (second column); Wavelet-based reconstructions contain noticeable noise in the background, and left some point-like artifact in the anatomical parts (third

column). Linear summation (forth column) and the proposed method (fifth column) perform similar where the background noise is eliminated and no point-like or staircase artifacts shown. The difference between the reconstruction and the reference image is shown in Fig. 5.8, correspondingly. In general, the last two columns show less structured artifacts, which indicates improved reconstructions.

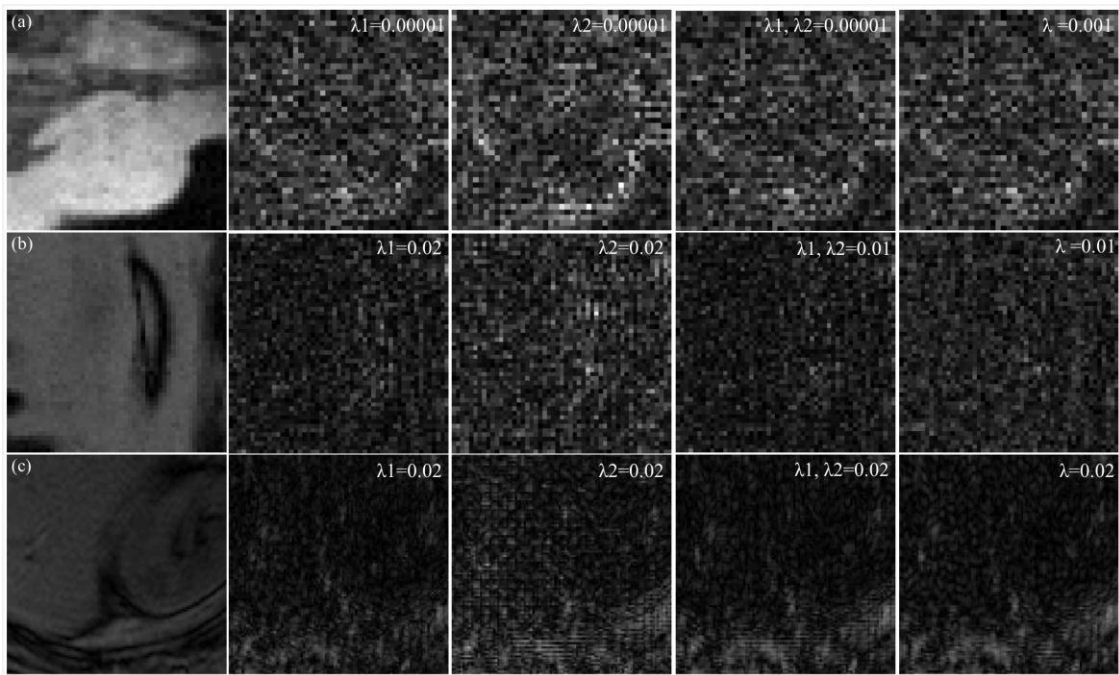


**Fig. 5.8** The error images between the reconstructed images and the reference images. The rows and columns correspond to those in Fig. 5.7.

Table 5-1 shows the quantitative NMSE of the four reconstruction methods. For wavelet, the best results (Daubechies 4 level 1) from trials with multiple filters and different filter length are tested, and the optimal one is used. From the NMSEs shown in

the table, the proposed method performs the best for the first and third data set, and the linear summation method performs the best for the second data set. Note that for the second data set, though the NMSE for linear summation is smaller than that of the proposed method, there is no visible difference between the two reconstructions.

*Table 5-1 Normalized mean square errors for finite-differences, wavelet, linear summation and the proposed method*

	<b>TV(Finite-difference)</b>	<b>Wavelet</b>	<b>Linear summation</b>	<b>Proposed method</b>
Breast	1.3e-6	3.9e-7	2.5e-7	<b>3.8e-8</b>
Brain	1.2e-4	2.8e-4	<b>8.1e-5</b>	1.4e-4
Abdomen	1.1e-6	8.3e-7	5.2e-7	<b>2.2e-7</b>

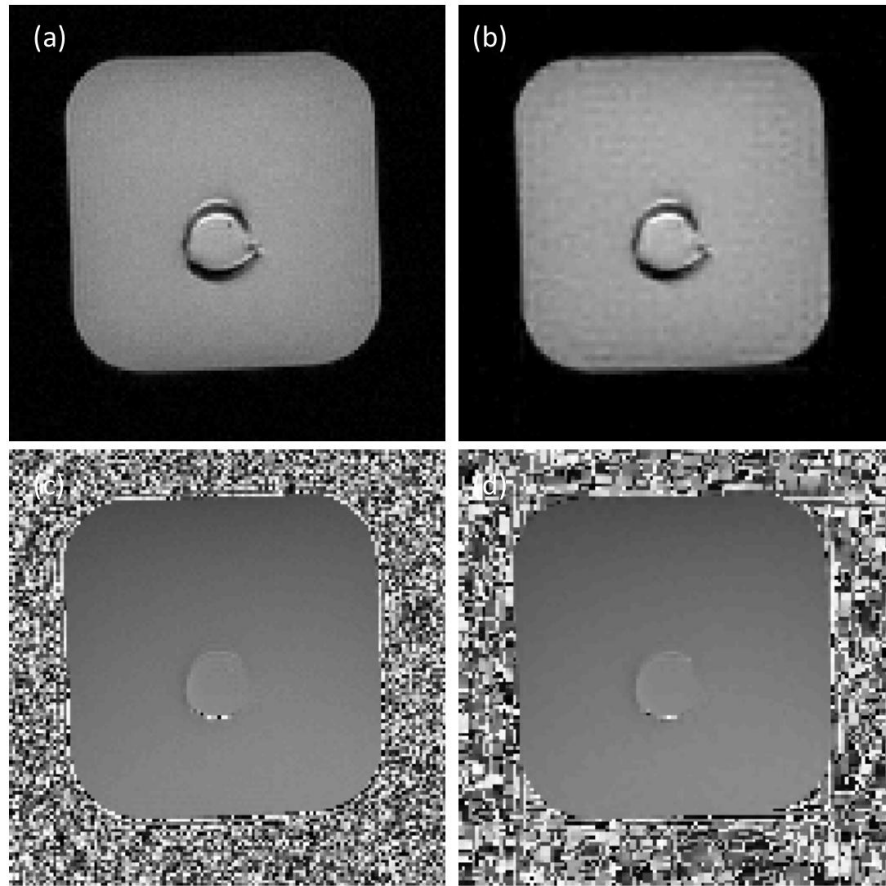
Table 5-2 shows the total reconstruction time using different methods. For finite-differences, wavelet and proposed method, each entry shows the total time spent on the 8 trial reconstructions. For linear summation, it is the total time of 64 reconstructions. It can be seen the proposed method requires much less time than linear summation time, and is on the same order as the wavelet-based reconstruction method.

*Table 5-2 Averaged single and total computational time (s) for finite-differences, wavelet, linear summation and the proposed method*

	<b>TV (Finite-difference)</b>	<b>Wavelet</b>	<b>Linear summation</b>	<b>Proposed method</b>
Breast	2.8 (22)	29.9 (239)	50.3 (3221)	21.5 (172)
Brain	37.3 (298)	122.9 (983)	167.5 (17021)	96.6 (773)
Abdomen	60.9 (487)	227.0 (2043)	546.4 (34967)	178.9 (1431)

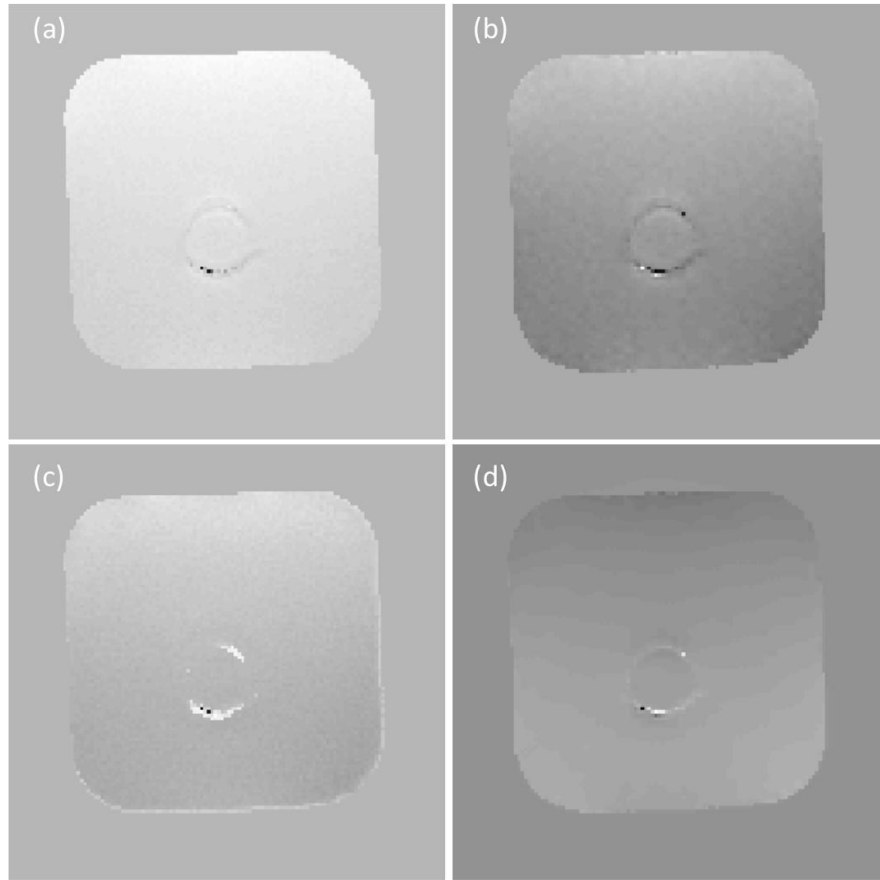
### ***5.2.5 Combined the compressive sensing and interventional devices localization***

Fig. 5.9 shows the magnitude and phase images of the center slice with  $T_{shift} = -0.3\text{ms}$ . Fig. 5.9 (a) and (c) shows the magnitude and phase image reconstructed using the full k-space data. Fig. 5.9 (b) and (d) shows the magnitude and phase image reconstructed using compressive sensing with 28% k-space data. From this comparison, it shows the compressive sensing can reconstruct the phase image with acceptable difference which can be potentially applied to the susceptibility mapping.



**Fig. 5.9** Magnitude (first row) and phase (second row) images of center slices with  $T_{\text{shift}} = -0.3\text{ms}$ , reconstructed with (first column) full k-space data, and (second column) 20 radial lines, which corresponding to 28% of total k-space data.





**Fig. 5.10 Field maps (first row) and susceptibility maps (second row) of center slices with  $T_{shift} = -0.3ms$ , reconstructed with (first column) full k-space data, and (second column) 20 radial lines, which corresponding to 28% of total k-space data.**

Fig. 5.10 shows the field maps and susceptibility images of the center slice with  $T_{shift} = -0.3ms$ . Fig. 5.10 (a) and (c) shows the field map and susceptibility image reconstructed using the full k-space data. Fig. 5.10(b) and (d) shows the field map and susceptibility image reconstructed using compressive sensing with 28% k-space data.

The susceptibility map reconstructed from compressive sensing shows some degradation of image quality, but it still can identify the location of the platinum wire.

### **5.3 Discussions**

Different wavelet filters and filter length lead to different reconstruction quality. Some of the wavelet filters may perform better than the others for a specific image. The reason is that if the images are fairly smooth, then short filters are not optimal. But longer wavelet filter will induce more correlation between adjacent coefficients, and limit the lowest frequency that can be resolved. In addition, different type of filters may have different energy leakage and ringing artifacts, which will lead to different reconstruction results in compressive sensing. Therefore, the performance of the wavelet method depends on the data and the choice of the filter. In our tests, a number of wavelets and filter lengths were tested and the optimal one were chosen based on the sparsifying power.

The conventional CS-MRI method with linear summations of different terms can provide the good reconstruction in terms of NMSE. However, it can be time-consuming to find the multiple, optimal regularization parameters for the two transforms. For the proposed method, it can provide comparable or better reconstructions in much less time. In addition, the proposed method is sparser in transform domain, therefore it converges faster.

The proposed method applies finite differences after the wavelet transform. An alternative way is to apply wavelet transform after finite differences. A further study

shows that the sequence of the sparsifying transforms does affect the results. However, the quality of the reconstructed image is not affected significantly. In terms of image quality, there seems to be no preference between the two. In terms of calculation time, applying finite differences first is faster than applying wavelet first. It is because for the later one, the wavelet has to be performed on two finite difference images, the horizontal and vertical images.

There are many possible combinations of the transforms to form the composite transform in the proposed method. In this paper, only the combination of finite-difference and wavelet transform is implemented and compared. Different combinations can provide a variety of new capability in handling different features. The proposed method can provide a large number of derivative sparsifying transforms that can be topics of research in specific applications.

Combined sparsifying transform inherits the advantages of each individual transform. Furthermore, the combinations can have its unique benefits. For example, Laplacian operator has been introduced as a new sparsifying transform [68]. Laplacian operator can be seen as a combination of two finite-differences. Even though finite-differences work well for piece-wise constant images, Laplacian can provide sparser representation for linear-changing images or even more rapid changing images. This means the proposed method is not only an alternative to linear summation method, but also a new avenue to build novel algorithms.

The long reconstruction time for conventional compressive sensing with wavelet transform and the proposed method is due to the slow wavelet transform. With other

transforms or even a wavelet transform with different filter type, the computational time can be much faster.

The simulated and experimental results have clearly shown that the high susceptibility will introduce severe image distortion to the images. Therefore, for some procedures that require accurate location of the susceptible objects, such as brachytherapy, marker insertion and biopsy, the visual assistance provided by conventional MRI is limited. The proposed method can be used to reduce the location error in these procedures with MRI imaging.

The  $180^\circ$  pulse can recover the phase induced by the field inhomogeneity after the spins are tipped down to x-y plane. However, the strong field variation induced by the high susceptible devices is in the same order of that induced by the selection gradients. Therefore, there still is a little phase variation across the phantom for  $T_{shift} = 0ms$ , as shown in the result. To overcome this, a 3D spin-echo sequence should be applied. However, the 3D spin-echo sequence takes much longer time and thus not practical for clinical applications.

To correctly calculate the field map, the phase difference between the two consecutive  $T_{shift}$  cannot exceed  $2\pi$ . Otherwise the phase unwrapping cannot correctly recover the phase change. This imposes a requirement on the  $\Delta T_{shift}$  selection. The rapid phase wrap due to the high susceptibility will introduce error. Though no accurate phase of the pixel on and at the immediate vicinity of the highly susceptible objects is required

for the calculation of the location. The study of  $T_{shift}$  selection will be one of our future researches.

Compressive sensing can be applied during the acquisition and reconstruction to reduce the acquisition time. Compressive sensing is not commonly used to reconstruct phase image. Compressive sensing utilizes k-space data and reconstruct complex image. Thus the phase image is available for free. The accuracy of the reconstructed phase image needs to be evaluated. However, it is good enough for our purpose which is to provide positive contrast and identify the location of interventional devices. Applying compressive sensing can significantly reduce the acquisition time. The disadvantage is that it increases reconstruction time. For the testing dataset whose dimension is  $128 \times 128 \times 9 \times 3$ , calculation time for each phase image using the method introduced in Chapter VI is about 30s (though it is much faster than linear summated method), resulting in 13.5min total time. Many methods can speed up the reconstruction time, such as using GPU or a faster algorithm, which is out of the scope of this paper.

## 5.4 Conclusions

In this chapter, we proposed a new compressive sensing MRI method that uses composite sparsifying transforms. Specifically, two or more sparsifying transforms are applied sequentially in the CS formulation. The method is tested using simulated reduced acquisition with three in-vivo data sets. The results show that the proposed method provides improved reconstruction quality than the conventional CS with a single transform, and similar or better quality as the conventional CS with linear summation of

multiple transforms. A unique benefit of the proposed method is that only one regularization parameter needs to be tuned. In practice, the proposed method can obtain optimal reconstruction significantly faster than the conventional CS-MRI with multiple transforms which requires tuning multiple parameters.

## CHAPTER VI

### CONCLUSIONS

In this thesis, we presented a new method to image highly susceptible interventional devices by mapping their susceptibility using a regularized  $L_1$  minimization.

The novelty of this thesis includes:

1. Phase unwrapping using Region-based Markov Random Field
2. Localization and visualization of interventional devices, such as brachytherapy seeds, platinum wire, and biopsy needle
3. Compressive sensing with composite sparsifying transform

The feasibility of the proposed method was demonstrated using phantom experiments and simulations. Preliminary results of MRI images with brachytherapy seeds, platinum wire and biopsy needle show that the proposed method can successfully localize and visualize interventional devices. To our best knowledge, this is the first time such mappings are done on interventional devices. Recommended shift values in a spin-echo sequence were identified. The potential of the method for providing positive-contrast device images instead of the conventional “black” or negative-contrast device images is very promising for interventional MRI. Improved visualization and localization were achieved using the proposed method. The proposed method can help increase the accuracy of the interventional procedures.

Further research on the following aspects to improve the proposed method will be done by my lab mates and collaborators:

1. Improving the acquisition speed by using compressive sensing, parallel imaging, and etc.;
2. Real time reconstruction by improving the algorithm, or using GPU;
3. Applying the proposed method to other interventional devices, such as stents.

In addition, the proposed method has the potential to be applied for other applications, such as localization and visualization of implanted devices, such as implanted joint.



## REFERENCES

- [1] P. R. Seevinck, H. de Leeuw, C. Bos, and C. J. Bakker, "Highly localized positive contrast of small paramagnetic objects using 3D center - out radial sampling with off - resonance reception," *Magn Reson Med*, vol. 65, pp. 146-156, 2011.
- [2] M. Stuber, W. D. Gilson, M. Schär, D. A. Kedziorek, L. V. Hofmann, S. Shah, *et al.*, "Positive contrast visualization of iron oxide - labeled stem cells using inversion - recovery with ON - resonant water suppression (IRON)," *Magn Reson Med*, vol. 58, pp. 1072-1077, 2007.
- [3] H. Dahnke, W. Liu, D. Herzka, J. A. Frank, and T. Schaeffter, "Susceptibility gradient mapping (SGM): A new postprocessing method for positive contrast generation applied to superparamagnetic iron oxide particle (SPIO) - labeled cells," *Magn Reson Med*, vol. 60, pp. 595-603, 2008.
- [4] G. Varma, R. E. Clough, P. Acher, J. Sénégas, H. Dahnke, S. F. Keevil, *et al.*, "Positive visualization of implanted devices with susceptibility gradient mapping using the original resolution," *Magn Reson Med*, vol. 65, pp. 1483-1490, 2011.
- [5] D. Formica and S. Silvestri, "Biological effects of exposure to magnetic resonance imaging: an overview," *Biomed Eng Online*, vol. 3, p. 11, 2004.
- [6] J. F. Schenck, "The role of magnetic susceptibility in magnetic resonance imaging: MRI magnetic compatibility of the first and second kinds," *Med Phys*, vol. 23, p. 815, 1996.
- [7] G. Whitehead and J. Ji, "Positive contrast MRI of prostate brachytherapy seeds based on resonant frequency offset mapping," in *2010 Annu Int Conf IEEE, Eng Med Biol Soc (EMBC)*, Buenos Aires, Argentina, 2010, pp. 6641-6644.
- [8] H. de Leeuw, P. Seevinck, and C. Bakker, "Center - out radial sampling with off - resonant reconstruction for efficient and accurate localization of punctate and elongated paramagnetic structures," *Magn Reson Med*, vol. 69, pp. 1611-1622, 2013.
- [9] T. Y. Siow, C.-C. V. Chen, C.-Y. Lin, J.-Y. Chen, and C. Chang, "MR phase imaging: sensitive and contrast-enhancing visualization in cellular imaging," *Magn Reson Imaging*, vol. 30, pp. 247-253, 2012.

- [10] L. De Rochefort, R. Brown, M. R. Prince, and Y. Wang, "Quantitative MR susceptibility mapping using piece - wise constant regularized inversion of the magnetic field," *Magn Reson Med*, vol. 60, pp. 1003-1009, 2008.
- [11] S. Chavez, Q.-S. Xiang, and L. An, "Understanding phase maps in MRI: a new outline phase unwrapping method," *Medical Imaging, IEEE Transactions on*, vol. 21, pp. 966-977, 2002.
- [12] K. Itoh, "Analysis of the phase unwrapping problem," *Appl. Opt*, vol. 21, p. 2470, 1982.
- [13] H. Zhong, S. Zhang, and J. Tang, "Path Following Algorithm for Phase Unwrapping Based on Priority Queue and Quantized Quality Map," in *Computational Intelligence and Software Engineering, 2009. CiSE 2009. International Conference on*, Wuhan, China, 2009, pp. 1-4.
- [14] M. Herráez, D. Burton, M. Lalor, and M. Gdeisat, "Fast two-dimensional phase-unwrapping algorithm based on sorting by reliability following a noncontinuous path," *Applied optics*, vol. 41, pp. 7437-7444, 2002.
- [15] D. C. Ghiglia and L. A. Romero, "Minimum  $L^p$ -norm two-dimensional phase unwrapping," *Journal of the Optical Society of America A*, vol. 13, pp. 1999-2013, 1996.
- [16] P. Ruiz, G. Kaufmann, and G. Galizzi, "Unwrapping of digital speckle-pattern interferometry phase maps by use of a minimum  $L^0$ -norm algorithm," *Applied optics*, vol. 37, pp. 7632-7644, 1998.
- [17] J. M. Francos and B. Friedlander, "The polynomial phase differencing algorithm for 2-D phase unwrapping: performance analysis," in *Acoustics, Speech, and Signal Processing, 1996. ICASSP-96. Conference Proceedings., 1996 IEEE International Conference on*, Atlanta, GA, 1996, pp. 2411-2414 vol. 4.
- [18] Z. P. Liang, "A model-based method for phase unwrapping," *Medical Imaging, IEEE Transactions on*, vol. 15, pp. 893-897, 1996.
- [19] J. Marroquin and M. Rivera, "Quadratic regularization functionals for phase unwrapping," *Journal of the Optical Society of America A*, vol. 12, pp. 2393-2400, 1995.
- [20] L. Guerriero, G. Nico, G. Pasquariello, and S. Stramaglia, "New regularization scheme for phase unwrapping," *Applied optics*, vol. 37, pp. 3053-3058, 1998.
- [21] D. C. Ghiglia and M. D. Pritt, *Two-dimensional phase unwrapping: theory, algorithms, and software*. New York, NY: Wiley 1998.

- [22] M. D. Pritt, "Comparison of path-following and least-squares phase unwrapping algorithms," in *Geoscience and Remote Sensing, 1997. IGARSS '97. Remote Sensing - A Scientific Vision for Sustainable Development., 1997 IEEE International*, Singapore, 1997, pp. 872-874 vol.2.
- [23] J. Strand and T. Taxt, "Performance evaluation of two-dimensional phase unwrapping algorithms," *Appl. Opt.*, vol. 38, pp. 4333-4344, 1999.
- [24] J. Dias and J. Leitaó, "The ZpiM algorithm for interferometric image reconstruction in SAR/SAS," *IEEE Transactions on Image processing*, vol. 11, p. 4, 2002.
- [25] J. M. Bioucas-Dias and G. Valadao, "Phase Unwrapping via Graph Cuts," *Image Processing, IEEE Transactions on*, vol. 16, pp. 698-709, 2007.
- [26] L. Ying, Z. P. Liang, D. C. Munson, Jr., R. Koetter, and B. J. Frey, "Unwrapping of MR phase images using a Markov random field model," *Medical Imaging, IEEE Transactions on*, vol. 25, pp. 128-136, 2006.
- [27] L. Ying, B. Frey, R. Koetter, and D. Munson, "An iterative dynamic programming approach to 2-D phase unwrapping," in *Image Processing, 2002 International Conference IEEE*, Rochester, NY, 2002, pp. 469-471.
- [28] R. Gonzalez and R. Woods, *Digital image processing*. Upper Saddle River, NJ: Prentice Hall, 2002.
- [29] J. L. Semmlow, *Biosignal and biomedical image processing: MATLAB-based applications* vol. 1. New York, NY: Taylor & Francis Inc, 2004.
- [30] L. Shapiro and G. Stockman, *Computer Vision*. Upper Saddle River, NJ: Prentice Hall, 2001.
- [31] C. Baker, K. King, D. Liang, and L. Ying, "Investigation of Sparsifying Transforms for Compressed Sensing in MRI Reconstruction," in *ISMRM*, Honolulu, HI, 2009.
- [32] H. Rue and L. Held, *Gaussian Markov random fields: theory and applications*. London, UK: Chapman & Hall, 2005.
- [33] S. Li, "Markov random field models in computer vision," in *Computer Vision—ECCV'94*, Sweden, 1994, pp. 361-370.
- [34] P. B. Chou and C. M. Brown, "The theory and practice of Bayesian image labeling," *International Journal of Computer Vision*, vol. 4, pp. 185-210, 1990.

- [35] P. V. Houdek, J. G. Schwade, A. J. Medina, C. A. Poole, K. R. Olsen, D. H. Nicholson, *et al.*, "MR technique for localization and verification procedures in episcleral brachytherapy," *Int J Radiat Oncol Biol Phys*, vol. 17, pp. 1111-1114, 1989.
- [36] D. McShan, R. Ten Haken, and B. Fraass, "3-D treatment planning: IV. Integrated brachytherapy planning," *Use Compute Radiat Ther*, pp. 249-252, 1987.
- [37] Y. Kyuma, A. Hayashi, K. Odakiri, and H. Nakamae, "Basic study on MRI guided stereotaxic surgery," *Neurol Surg*, vol. 17, p. 449, 1989.
- [38] A. V. D'Amico, R. Cormack, S. Kumar, and C. M. Tempany, "Real-time magnetic resonance imaging-guided brachytherapy in the treatment of selected patients with clinically localized prostate cancer," *J endourology*, vol. 14, pp. 367-370, 2000.
- [39] C. Ménard, R. C. Susil, P. Choyke, G. S. Gustafson, W. Kammerer, H. Ning, *et al.*, "MRI-guided HDR prostate brachytherapy in standard 1.5 T scanner," *Int J Radiat Oncol Biol Phys*, vol. 59, pp. 1414-1423, 2004.
- [40] M. Miquel, K. Rhode, P. Acher, N. Macdougall, J. Blackall, R. Gaston, *et al.*, "Using combined x-ray and MR imaging for prostate I-125 post-implant dosimetry: phantom validation and preliminary patient work," *Phys Med Biol*, vol. 51, p. 1129, 2006.
- [41] K. Wachowicz, S. Thomas, and B. Fallone, "Characterization of the susceptibility artifact around a prostate brachytherapy seed in MRI," *Med Phys*, vol. 33, p. 4459, 2006.
- [42] V. Lagerburg, M. Moerland, J. Seppenwoolde, and J. Lagendijk, "Simulation of the artefact of an iodine seed placed at the needle tip in MRI-guided prostate brachytherapy," *Phys Med Biol*, vol. 53, p. N59, 2008.
- [43] S. Thomas, K. Wachowicz, and B. Fallone, "MRI of prostate brachytherapy seeds at high field: A study in phantom," *Med Phys*, vol. 36, p. 5228, 2009.
- [44] L. De Rochefort, T. Liu, B. Kressler, J. Liu, P. Spincemaille, V. Lebon, *et al.*, "Quantitative susceptibility map reconstruction from MR phase data using bayesian regularization: validation and application to brain imaging," *Magn Reson Med*, vol. 63, pp. 194-206, 2010.
- [45] B. Kressler, L. de Rochefort, T. Liu, P. Spincemaille, Q. Jiang, and Y. Wang, "Nonlinear regularization for per voxel estimation of magnetic susceptibility

- distributions from MRI field maps," *IEEE Trans Med Imaging*, vol. 29, pp. 273-281, 2010.
- [46] J. Liu, T. Liu, L. de Rochefort, J. Ledoux, I. Khalidov, W. Chen, *et al.*, "Morphology enabled dipole inversion for quantitative susceptibility mapping using structural consistency between the magnitude image and the susceptibility map," *Neuroimage*, vol. 59, pp. 2560-2568, 2012.
- [47] B. Wu, W. Li, A. Guidon, and C. Liu, "Whole brain susceptibility mapping using compressed sensing," *Magn Reson Med*, vol. 67, pp. 137-147, 2012.
- [48] Y. Dong, Z. Chang, G. Whitehead, and J. Ji, "Localization of brachytherapy seeds in MRI by deconvolution," presented at the 2013 Annu Int Conf IEEE, Eng Med Biol Soc (EMBC), Osaka, Japan, 2013.
- [49] Q. Liu, S. Wang, X. Peng, and D. Liang, "Adaptive Two-level Sparsifying Transform for Compressed Sensing MRI," presented at the EMBC, Osaka, Tokyo, 2013.
- [50] J. Marques and R. Bowtell, "Application of a Fourier - based method for rapid calculation of field inhomogeneity due to spatial variation of magnetic susceptibility," *Concepts in Magn Reson*, vol. 25, pp. 65-78, 2005.
- [51] Y.-C. N. Cheng, J. Neelavalli, and E. M. Haacke, "Limitations of calculating field distributions and magnetic susceptibilities in MRI using a Fourier based method," *Phys Med Biol*, vol. 54, p. 1169, 2009.
- [52] J. Du, M. Carl, and G. M. Bydder, "Ultrashort TE imaging: phase and frequency mapping of susceptibility effects in short T2 tissues of the musculoskeletal system," in *Susceptibility weighted imaging in MRI: basic concepts and clinical applications*, E. M. Haacke and J. R. Reichenbach, Eds., ed Hoboken, NJ: John Wiley & Sons, Inc., 2011, pp. 669-696.
- [53] D. A. Yablonskiy and E. M. Haacke, "An MRI method for measuring T2 in the presence of static and RF magnetic field inhomogeneities," *Magn Reson Imaging*, vol. 37, pp. 872-876, 1997.
- [54] J. Ma and F. W. Wehrli, "Method for image-based measurement of the reversible and irreversible contribution to the transverse-relaxation rate," *J Magn Reson*, vol. 111, pp. 61-69, 1996.
- [55] T. Liu, J. Liu, L. de Rochefort, P. Spincemaille, I. Khalidov, J. R. Ledoux, *et al.*, "Morphology enabled dipole inversion (MEDI) from a single - angle acquisition: Comparison with COSMOS in human brain imaging," *Magn Reson Med*, vol. 66, pp. 777-783, 2011.

- [56] J. Li, S. Chang, T. Liu, Q. Wang, D. Cui, X. Chen, *et al.*, "Reducing the object orientation dependence of susceptibility effects in gradient echo MRI through quantitative susceptibility mapping," *Magn Reson Med*, vol. 68, pp. 1563-1569, 2012.
- [57] M. Lustig, D. Donoho, and J. M. Pauly, "Sparse MRI: The application of compressed sensing for rapid MR imaging," *Magn Reson Med*, vol. 58, pp. 1182-1195, 2007.
- [58] A. S. Kirov and J. F. Williamson, "Monte Carlo-aided dosimetry of the Source Tech Medical Model STM1251 I-125 interstitial brachytherapy source," *Med phys*, vol. 28, p. 764, 2001.
- [59] Y. Yu, L. L. Anderson, Z. Li, D. E. Mellenberg, R. Nath, M. Schell, *et al.*, "Permanent prostate seed implant brachytherapy: report of the American Association of Physicists in Medicine Task Group No. 64," *Med phys*, vol. 26, pp. 2054-2076, 1999.
- [60] S. Liu, J. Neelavalli, Y. C. N. Cheng, J. Tang, and E. Mark Haacke, "Quantitative susceptibility mapping of small objects using volume constraints," *Magn Reson Med*, vol. 69, pp. 716-723, 2013.
- [61] Y. Dong and J. Ji, "Novel compressive sensing mri methods with combined sparsifying transforms," in *Biomedical and Health Informatics (BHI), 2012 IEEE-EMBS International Conference on*, Hong Kong, China, 2012, pp. 721-724.
- [62] E. Candès, "The restricted isometry property and its implications for compressed sensing," *Comptes Rendus Mathematique*, vol. 346, pp. 589-592, 2008.
- [63] S. Boyd and L. Vandenberghe, *Convex optimization*. Cambridge, England: Cambridge Univ Pr, 2004.
- [64] K. Engan, S. O. Aase, and J. Hakon Husoy, "Method of optimal directions for frame design," in *Acoustics, Speech, and Signal Processing, 1999. Proceedings., 1999 IEEE International Conference on*, Phoenix, AZ, 1999, pp. 2443-2446.
- [65] M. Aharon, M. Elad, and A. Bruckstein, "k-svd: An algorithm for designing overcomplete dictionaries for sparse representation," *Signal Processing, IEEE Transactions on*, vol. 54, pp. 4311-4322, 2006.
- [66] M. Do and M. Vetterli, "The contourlet transform: an efficient directional multiresolution image representation," *Image Processing, IEEE Transactions on*, vol. 14, pp. 2091-2106, 2005.

- [67] E. Candes and D. Donoho, *Curvelets: A surprisingly effective nonadaptive representation for objects with edges*. Stanford, CA: Stanford University, 1999.
- [68] Y. Dong and J. Ji, "Compressive sensing MRI with laplacian sparsifying transform," in *IEEE Int. Symp. Biomedical Imaging: From Nano to Macro* Chicago, IL, 2011, pp. 81-84.
- [69] F. Knoll, K. Bredies, T. Pock, and R. Stollberger, "Second order total generalized variation (TGV) for MRI," *Mag Reson Med*, pp. 480-491, 2011.
- [70] J. L. Starck, M. Elad, and D. L. Donoho, "Image decomposition via the combination of sparse representations and a variational approach," *Image Processing, IEEE Transactions on*, vol. 14, pp. 1570-1582, 2005.
- [71] X. Qu, X. Cao, D. Guo, C. Hu, and Z. Chen, "Combined sparsifying transforms for compressed sensing MRI," *Electronics letters*, vol. 46, pp. 121-123, 2010.
- [72] C. Chen, J. Huang, and A. Leon, "Accelerated parallel magnetic resonance imaging with combined gradient and wavelet sparsity," in *In Proc. of the 26th Annual Conference on Neural Information Processing Systems (NIPS)*, Lake Tahoe, NV, 2012.
- [73] G. Plonka and J. Ma, "Curvelet-wavelet regularized split Bregman iteration for compressed sensing," *preprint*, vol. 18, 2011.
- [74] X. Qu, X. Cao, C. Hu, and Z. Chen, "Compressed sensing MRI with combined sparsifying transforms and smoothed l0 norm minimization," in *Proc. IEEE Int Conf. Acoustics, Speech & Sig. Proc., ICASSP*, Dallas, TX, 2010, pp. 626-629.
- [75] A. Sbrizzi, H. Hoogduin, J. J. Lagendijk, P. Luijten, G. L. G. Sleijpen, and C. A. A. v. d. Berg, "Time efficient design of multi dimensional RF pulses: application of a multi shift CGLS Algorithm," *Mag Reson Med*, pp. 879-885, 2011.
- [76] R. Chartrand, "Fast algorithms for nonconvex compressive sensing: MRI reconstruction from very few data," in *Biomedical Imaging: From Nano to Macro*, Boston, MA, 2009, pp. 262-265.
- [77] M. Lustig, D. L. Donoho, J. M. Santos, and J. M. Pauly, "Compressed sensing MRI," *Signal Processing Magazine, IEEE*, vol. 25, pp. 72-82, 2008.
- [78] J. Ma, "Improved Iterative Curvelet Thresholding for Compressed Sensing," *preprint*, 2009.

- [79] M. Guerquin-Kern, M. Haberlin, K. Pruessmann, and M. Unser, "A Fast Wavelet-Based Reconstruction Method for Magnetic Resonance Imaging," *Medical Imaging, IEEE Transactions on*, vol. 30, pp. 1649-1660, 2011.
- [80] J. Buckheit, S. Chen, D. Donoho, I. Johnstone, and J. Scargle, "About wavelab," ed, 2005, pp. 1-39.